

# Bayesian inversion of joint SH seismic and seismoelectric data to infer glacier system properties

Franco Macchioli-Grande<sup>1\*</sup>, Fabio Zyserman<sup>1</sup>, Leonardo Monachesi<sup>2</sup>,  
Laurence Jouniaux<sup>3</sup> and Marina Rosas-Carbajal<sup>4</sup>

<sup>1</sup>CONICET, Facultad de Ciencias Astronómicas y Geofísicas, Universidad Nacional de La Plata, B1900 FWA, La Plata, Buenos Aires, Argentina, <sup>2</sup>CONICET, Instituto de Investigación en Paleobiología y Geología, Universidad Nacional de Río Negro, General Roca Río Negro 8332, Argentina, <sup>3</sup>Institut de Physique du Globe de Strasbourg (UMR 7516), Université de Strasbourg et CNRS, Strasbourg, Grand Est 67084, France, and <sup>4</sup>Institut de Physique du Globe de Paris, CNRS, UMR 7154, Université de Paris, Paris, France

Received July 2019, revision accepted January 2020

## ABSTRACT

In glacial studies, properties such as glacier thickness and the basement permeability and porosity are key to understand the hydrological and mechanical behaviour of the system. The seismoelectric method could potentially be used to determine key properties of glacial environments. Here we analytically model the generation of seismic and seismoelectric signals by means of a shear horizontal seismic wave source on top of a glacier overlying a porous basement. Considering a one-dimensional setting, we compute the seismic waves and the electrokinetically induced electric field. We then analyse the sensitivity of the seismic and electromagnetic data to relevant model parameters, namely depth of the glacier bottom, porosity, permeability, shear modulus and saturating water salinity of the glacier basement. Moreover, we study the possibility of inferring these key parameters from a set of very low noise synthetic data, adopting a Bayesian framework to pay particular attention to the uncertainty of the model parameters mentioned above. We tackle the resolution of the probabilistic inverse problem with two strategies: (1) we compute the marginal posterior distributions of each model parameter solving multidimensional integrals numerically and (2) we use a Markov chain Monte Carlo algorithm to retrieve a collection of model parameters that follows the posterior probability density function of the model parameters, given the synthetic data set. Both methodologies are able to obtain the marginal distributions of the parameters and estimate their mean and standard deviation. The Markov chain Monte Carlo algorithm performs better in terms of numerical stability and number of iterations needed to characterize the distributions. The inversion of seismic data alone is not able to constrain the values of porosity and permeability further than the prior distribution. In turn, the inversion of the electric data alone, and the joint inversion of seismic and electric data are useful to constrain these parameters as well as other glacial system properties. Furthermore, the joint inversion reduces the uncertainty of the model parameters estimates and provides more accurate results.

**Key words:** Electromagnetics, Inversion, Modelling, Parameter Estimation, Seismics.

## 1 INTRODUCTION

Seismoelectromagnetics aims at combining the well-established seismic method with the sensitivity of

---

\*E-mail: fmacchio@fcaglp.unlp.edu.ar

electromagnetic methods to fluid content in porous rocks to study the subsurface. Seismoelectric and electroseismic signals originate from the electrokinetic coupling phenomenon (Overbeek 1952; Jouniaux and Zyserman 2016). The seismoelectric method uses a seismic source to induce a relative motion between the fluid and the rock matrix. This relative motion results in an equivalent current density, which leads to an electromagnetic field accompanying the seismic wave propagation. Seismoelectric signals with non-negligible amplitudes can also arise at interfaces of media with different electrokinetic or seismic properties (Haartsen and Pride 1997; Garambois and Dietrich 2002). At such interfaces, the electric current density is unbalanced, inducing an electric dipole and thus an electric field propagating at the speed of the light in the medium, which may be detected at the surface (Pride and Garambois 2005; Haines and Pride 2006). Recent theoretical works predict the existence of seismoelectric conversions due to heterogeneities and meso-scale fractures in porous media (Jougnot *et al.* 2013; Monachesi *et al.* 2015). The seismoelectric method can be performed using either a natural source (earthquakes) or an active seismic source. Very recent works illustrate the potential of both types of sources. Dzieran *et al.* (2019) studied the influence of the interface response (IR) on seismoelectric signals arising from earthquake sources. By introducing the seismoelectric spectral ratio (SESR), they analysed field and synthetic data leaving behind the source signature and showed that the SESR depends on the frequency due to the presence of the IR. Moreover, this dependence is related to the hydrogeological setting through the variation of parameters such as porosity and salinity. Butler, Kulesa and Pugin (2018) performed a field study using explosive and vibroseis sources in clayey sediments and observed quasi-coseismic seismoelectric arrivals, characterized as evanescent electromagnetic waves (Ren, Huang and Chen 2016, 2018), generated by the arrival of reflected P and S waves at the top of a shallow layer of elevated porosity and electrical conductivity. The performance of such study in a region with known geological structure allows to broaden the amount of information able to be extracted from seismoelectric signals.

Other recent works in the lively research realm of seismoelectrics comprise results in theory (Jardani and Revil 2015; Grobbo and Slob 2016; Munch and Zyserman 2016; Fiorentino, Toussaint and Jouniaux 2017; Gao, Huang and Hu 2017a,b; Zyserman, Monachesi and Jouniaux 2017a,b; Dietrich *et al.* 2018; Guan, Shi and Hu 2018; Monachesi, Zyserman and Jouniaux 2018a; Gao *et al.* 2019) as well as from laboratory tests (Bordes *et al.* 2015; Hu, Wang and Guan 2015; Holzhauser *et al.* 2017; Peng *et al.* 2017; Devi *et al.*

2018). A detailed account of results on most topics of interest in seismoelectrics can be found in the review of Jouniaux and Zyserman (2016) and in the book by Revil *et al.* (2015).

Characterizing glacier system properties has been a matter of interest in the field of electric and electromagnetic prospecting methods throughout the last two decades. Glaciers are fragile systems highly responsive to climate variations. Studying physical properties of glaciers and their evolution in time can help to better understand the global hydrological balance and the variations in the sea level resulting from glacier mass changes. In this context, the seismoelectric method appears as a potential utility in glacial studies. Because the method is sensitive to mechanical and electromagnetic properties, it may allow an in-depth characterization of glacier environments in terms of structure and temporal evolution of the system. Regarding seismoelectric studies on glaciers, Kulesa, Murray and Rippin (2006) recorded seismoelectric signals on Glacier de Tsanfleuron, Switzerland, using a single channel vertical sounding geometry. They inferred the electromagnetic waves to be generated by electrokinetic conversion of seismic waves within the snow pack and near the dry-wet ice and ice-bed interfaces. In laboratory tests, Liu *et al.* (2008) showed that an electric double layer is formed at the boundary between permafrost and unfrozen soil, and observed seismoelectric conversions originated there due to the electric and mechanical contrasts between both media. On the other hand, Zyserman, Gauzellino and Santos (2012) predicted electroseismic conversions at the same interface in a numerical study of methane-hydrate reservoirs. Later, Mahardika (2013) was able to produce numerical synthetic data compatible with the field recordings collected by Kulesa *et al.* (2006), treating the snow-glacial environment in a similar way as he did with the vadose zone-aquifer zone in an unsaturated porous medium (Revil and Mahardika 2013). Quite recently, Siegert *et al.* (2018) interpreted, from seismoelectric soundings of the West Greenland Ice Sheet, arrival times from the till layer beneath the ice-sheet base fully compatible with previous data obtained with seismic amplitude variation with offset surveys. Although convincing multi-channel measurements have yet to be acquired on ice, the aforementioned publications encourage the study of glacier systems using seismoelectrics. A recent theoretical study by Monachesi, Zyserman and Jouniaux (2018b) showed that the electromagnetic interface response originating at the interface between the glacier bottom and the basement is proportional to the electric current density at this depth, and depends on textural and electrical properties that could be of interest to characterize glacial systems. This study, however, did not address whether these

parameters may be recovered in a seismoelectric acquisition scenario, and with which degree of uncertainty.

In subsurface geophysics, the determination of key parameters of the system under study is done through the resolution of an inverse problem (Mosegaard and Tarantola 2002). The data inversion is tackled using either a deterministic or a probabilistic (also known as Bayesian) approach. Deterministic inversion searches for a single, optimal set of model parameters, whereas probabilistic inversion aims at characterizing a full probability density function (pdf) of these parameters. The latter provides a more complete information on the models that are more likely to explain our data set (Tarantola and Valette 1982). Geophysical phenomena can be described in terms of a joint probability distribution of a large set of variables, but if we are interested in the behaviour of a specific variable, we turn to marginal distributions. They can be obtained by integration or sampling of the pdf of the model parameters given a certain data set – the posterior pdf (see Section 5 for a thorough insight).

The existing literature on inversion of seismoelectric data is not, to our knowledge, very broad. Concerning deterministic studies, it is worth to mention the works of Guan, Hu and Wang (2013), Chen and Yang (2013) and Bonnetier, Triki and Xue (2019), which deal with an electrolyte-saturated homogeneous poroelastic medium. Guan *et al.* (2013) successfully determined the permeability of different fluid saturated homogeneous porous formations from seismoelectric well logs, deriving the amplitude ratio of electric signal to acoustic pressure of Stoneley waves, and obtaining the permeability from an expression involving the tangent of its phase. They determined the conditions under which the electric conductivity and the electrokinetic coupling coefficient can be recovered from a two-step inversion. On the other hand, Chen and Yang (2013) and Bonnetier *et al.* (2019) carried out a stability analysis of the inverse problem for the possible recovery of the same two parameters from knowledge of the seismoelectric fields. Concerning the probabilistic approach, Jardani *et al.* (2010) performed a stochastic joint inversion procedure of synthetic seismic and seismoelectric data using an Adaptive Metropolis algorithm. They modelled the seismoelectric response over a two-dimensional stratified medium hosting a reservoir partially saturated with oil employing a finite element algorithm. They were able to retrieve information about the different geological units of the model, comprising permeability, porosity, electrical conductivity, bulk modulus of the dry porous frame, bulk modulus of the pore fluid, bulk modulus of the solid phase and shear modulus of the formations. They were able to recover the permeability within

one order of magnitude, electrical conductivity and other material properties, with the exception of the porosity, which was not well constrained by the inversion. Although the obtained distributions are mostly centred around the true values, they show large dispersion, even in logarithmic scale. More recently, Mahardika, Revil and Jardani (2012); Mahardika (2013), employing a similar approach, performed an inversion of synthetic data corresponding to the occurrence of a fracking event in a two-layered system. The authors concluded that when using noiseless data, its electric portion contains more information than the seismic one, and that the model parameters obtained via joint inversion are more accurate than the ones obtained by inverting the seismic time-series alone.

In the present paper, we propose a Bayesian framework to analyse the information that can be recovered about relevant model parameters of a glacial environment. On the one hand, we calculate the marginal distribution of each model parameter computing multidimensional integrals. We numerically compute the latter by means of the Cuba library (Hahn 2005), which offers a variety of Monte Carlo and deterministic methods. On the other hand, we solve the probabilistic inverse problem using a Markov chain Monte Carlo algorithm (MCMC): the Differential Evolution Adaptive Metropolis (DREAM) (Vrugt *et al.* 2009). This is a highly optimized algorithm that combines the capability of MCMC methods of ensuring convergence to the target distribution (Tarantola 2005) with features of Differential Evolution algorithms (Sambridge and Drijkoningen 1992; Sen and Stoffa 1992) which allows a proper scale and orientation of the proposal distribution employed to sample the posterior pdf. This approach results in a collection of model parameters that follow the posterior pdf. Histograms of the marginal distributions and the uncertainty estimates can be computed from such collection.

The resolution of the inverse problem requires the computation of the forward model, which in our case permits to simulate the seismic and seismoelectric data. Specifically, we simulate full waveform primary and multiple reflections and interfacial effects from the base of the ice. We calculate them following the analytic expressions for the electric field and seismic waves obtained by Monachesi *et al.* (2018b), assuming a one-dimensional geometry. The seismoelectric theoretical framework used in the forward modelling is the one presented by Pride (1994), broadly used in seismoelectric studies (Garambois and Dietrich 2002; Hu, Guan and Harris 2007; Haines, Guitton and Biondi 2007a,b; Hu and Gao 2011; Warden *et al.* 2012; Zyserman *et al.* 2012; Guan *et al.* 2013; Warden *et al.* 2013; Kröger, Yaramanci and Kemna 2014;

Bordes *et al.* 2015; Zyserman *et al.* 2015; Gao, Huang and Hu 2017a; Zyserman *et al.* 2017a; Guan *et al.* 2018). The solutions we employ were derived under a set of assumptions, such as the consideration of the glacier as an elastic uniform medium (no liquid content), uniform properties through the entire ice sheet and the basement and a planar shear wave source applied over the entire ice surface at once. The use of an shear horizontal (SH) source permits a higher signal-to-noise ratio (SNR) than when using compressional sources (Zyserman *et al.* 2017a). This source has been lately successfully used in several shallow subsurface studies, both theoretical seismoelectric ones and seismic field works (see Monachesi *et al.* 2018b and references therein). In addition, Polom *et al.* (2014) were able to identify the depth of a glacier basement, and structures below, by inverting both P- and SH-wave data. They remarked that unexpectedly they were able to retrieve information from the S-wave in the studied environment.

The synthetic data are generated adding a noise term to the seismic and seismoelectric noiseless data. The former is generated following noise generation standards for seismic and electromagnetic data, respectively. That is, for the seismic signal, the noise term is constant and dependent of the SNR (Robinson and Treitel 2000), whereas for the electric field signal, the noise term is proportional to the noiseless signal amplitude (Chen *et al.* 2007; Kalscheuer *et al.* 2010; Rosas-Carbajal *et al.* 2014).

The reminder of this paper is structured as follows: Section 2 comprises the formulation of the equations for the seismoelectric problem in a glacial environment. Section 3 details the model parameters we are interested in studying, and Section 4 explains how the synthetic data are computed. Section 5 presents the principles of Bayesian inference applied to our problem, and the methodology used to compute the posterior marginal probabilities and the full posterior pdf distribution using an MCMC scheme. In Section 6, we present the main results in terms of a sensitivity analysis and the Bayesian inference with the aforementioned techniques. Finally, Section 7 discusses the results and their contribution to the study of glacier environments, and Section 8 outlines the main findings and conclusions.

## 2 FORWARD MODEL

Following Monachesi *et al.* (2018b), we assume a one-dimensional medium constituted by a single layer on top of a half-space in contact at a given depth denoted by  $z_b$  (see Fig. 1). The top layer represents the ice body of the glacier, and is assumed to be an elastic medium, whereas the half-

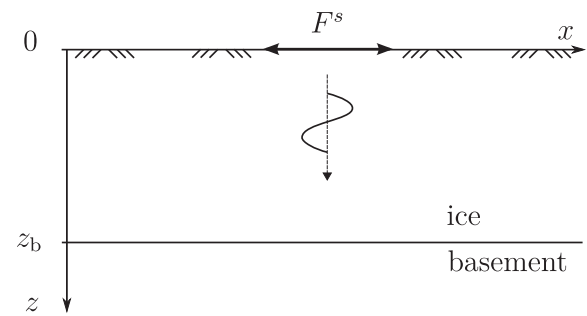


Figure 1 Schematic representation of the one-dimensional system considered in this study. The ice body is assumed to be an elastic medium, whereas the porous basement is treated as a poroelastic medium.

space represents the glacier basement, which we assume to be a porous medium fully saturated with water. The seismic source of the system, located at the glacier surface, is a shearing force, parallel to the  $x$ -axis acting on a horizontal infinite plane. Under these assumptions, the source can only induce displacements in the  $x$ -direction, with amplitudes depending only on depth.

The mechanical equation that governs the wave propagation in the glacier, written in the space-frequency domain, assuming an  $e^{i\omega t}$  time dependence, is given by (Aki and Richards 2002):

$$-\omega^2 \rho_{\text{ice}} u_x - G_{\text{ice}} \frac{\partial^2 u_x}{\partial z^2} = F^s(\omega) \delta(z), \quad (1)$$

where  $\omega$  is the angular frequency,  $\rho_{\text{ice}}$  and  $G_{\text{ice}}$  stand for the mass density and the shear modulus of the ice composing the glacier and  $u_x$  is the displacement. The right-hand side of equation (1) represents the shearing source acting on the surface ( $z = 0$ ),  $F^s(\omega)$  is the shearing force per unit area and  $\delta(z)$  is the Dirac delta function.

In order to model the seismoelectric response, we assume that the net electric charge in the whole domain is zero and the magnetic permeability is the one of the vacuum. With these assumptions, the electric and magnetic fields in the glacier will satisfy the following simplified form of Maxwell's equations:

$$-\sigma_{\text{ice}} E_x - \frac{\partial H_y}{\partial z} = 0, \quad (2)$$

$$\frac{\partial E_x}{\partial z} + i\omega \mu_0 H_y = 0, \quad (3)$$

where  $E_x$  and  $H_y$  are the electric and magnetic fields, respectively,  $\sigma_{\text{ice}}$  is the electric conductivity of the glacier and  $\mu_0 = 4\pi \times 10^{-7} \text{ N A}^{-2}$  is the vacuum magnetic permeability. Note that the displacement currents are not accounted for

in equations (2) and (3); this is the common assumption for shallow seismoelectric surveys (Hu and Liu 2002; Haines and Pride 2006; Bordes *et al.* 2015; Gao, Huang and Hu 2017a; Guan *et al.* 2018). This form of Maxwell's equations is commonly known as magneto quasi-static approximation. It has been analysed within the frame of seismoelectrics in the last two mentioned references, and previously by other authors (Løseth *et al.* 2006; Rapetti and Rousseaux 2014) in more general contexts.

To model the seismoelectric response in the basement, we use the equations derived by Pride (1994). If the electroosmotic feedback is neglected in Biot's equations, as it is usually assumed for frequencies that vary from 10 Hz to 1 kHz, range of interest for shallow seismoelectric surveys (tens to hundreds of meters) (Hu and Liu 2002; Haines and Pride 2006; Warden *et al.* 2013; Bordes *et al.* 2015; Gao, Huang and Hu 2017a; Guan *et al.* 2018), Pride's equations can be written as follows:

$$-\omega^2 \rho_b \mathbf{u}_{s,x} - \omega^2 \rho_w \mathbf{u}_{f,x} - G_b \frac{\partial^2 \mathbf{u}_{s,x}}{\partial z^2} = 0, \quad (4)$$

$$-\omega^2 \rho_w \mathbf{u}_{s,x} - \omega^2 g_0 \mathbf{u}_{f,x} + i\omega \frac{\eta_w}{\kappa} \mathbf{u}_{f,x} = 0, \quad (5)$$

$$-\sigma_b E_x - \frac{\partial H_y}{\partial z} = i\omega \frac{\eta_w}{\kappa} L_0 \mathbf{u}_{f,x} = j_v, \quad (6)$$

$$\frac{\partial E_x}{\partial z} + i\omega \mu_0 H_y = 0. \quad (7)$$

In these equations,  $\mathbf{u}_{s,x}$  and  $\mathbf{u}_{f,x}$  are the average solid and relative fluid displacements, respectively,  $\rho_b$  is the bulk mass density, which can be computed as  $\rho_b = \rho_s(1 - \phi) + \phi\rho_w$ , being  $\rho_s$  the mass density of the solid grains constituting the basement porous matrix,  $\rho_w$  the mass density of water and  $\phi$  the porosity of the medium.  $G_b$  is the basement rock matrix shear modulus,  $g_0$  the Biot's low frequency inertial coupling coefficient, computed as  $g_0 = F\rho_w$  (Santos *et al.* 2004, 2005; Zyserman *et al.* 2012), where  $F$  is the formation factor given by  $F = \phi^{-\hat{m}}$ , being  $\hat{m}$  the cementation exponent,  $\eta_w$  is the water viscosity and  $\kappa$  the permeability of the porous rock matrix. The right-hand side in equation (6) is the electric current density, source of the electromagnetic signals, and can be referred to as the viscous current density  $j_v$ , whereas  $\sigma_b E_x$  is the conduction current,  $\sigma_b$  being the electric conductivity of the basement. The coefficient  $L_0$  is the electrokinetic coupling (Pride 1994); it creates, in this model, the coupling between the seismic wave and the electric and magnetic fields. If this coupling is zero, there are no seismo-electromagnetic conversions. Within the seismic frequency band, it can be

written as (Pride 1994; Warden *et al.* 2013; Bordes *et al.* 2015):

$$L_0 = -\frac{\epsilon_w \zeta}{\eta_w F} \left(1 - 2\frac{d}{\Lambda}\right), \quad (8)$$

where  $\zeta$  is the zeta potential and  $\epsilon_w$  is the permittivity of water,  $d$  the Debye length and  $\Lambda$  a geometrical parameter, related to the matrix pore structure.

In order to solve the problem stated by equations (1)–(7), it is necessary to establish boundary conditions for the displacements and the electromagnetic fields, both in the boundaries of the system ( $z = 0$  and  $z \rightarrow \infty$ ) and at the interface between both media ( $z = z_b$ ). Once the boundary conditions are stated, the problem can be analytically solved taking advantage of the decoupling of the mechanical and electromagnetic equations; we first solve the mechanical problem and, then, the obtained solution is used to derive the final solutions for the electric and magnetic fields. Their final expressions are given in the Appendix; the full derivation is detailed in Monachesi *et al.* (2018b).

### 3 MODEL PARAMETERS

We first present the subsurface model parameters that we are interested in characterizing and those we assume to be known in advance. Then we describe the rock physics models published in the literature which we use to relate our unknown model parameters to others needed to solve the forward problem. In the previous section, we established that both the glacier and the basement are homogeneous. As in a geophysical survey we have direct access to the ice, we consider known – and constant – all its relevant parameters (see values in Table 1). The ice shear modulus is computed as  $G_{ice} = v_{ice}^2 \rho_{ice}$ .

Therefore, we consider the basement parameters listed in Table 1 as the free ones (the ones to be determined by an inversion procedure are in boldface). Other parameters, independent of the listed ones but considered to remain constant, are the water viscosity  $\eta_w$  and the water electric permittivity  $\epsilon_w$ . The water viscosity is not expected to change significantly from the chosen value (see Table 1) due to the studied geological setting, whereas the electric permittivity could in principle be considered as a possible free model parameter. However, as it can be seen in Gueguen and Palciauskas (1994, Fig. IX.7), for temperatures near and above 0°C,  $\epsilon_w$  remains almost constant. Consequently, we considered  $\epsilon_w$  to be constant, and used  $\epsilon_w = 85\epsilon_0$  (Gueguen and Palciauskas 1994) in this work.

**Table 1** Values of model parameters used in the present study

Model Parameters			
Glacier Ice			
Density, $\rho_{\text{ice}}$ [kg m <sup>-3</sup> ]	900*	S-wave phase velocity, $v_{\text{ice}}$ [m s <sup>-1</sup> ]	1800*
Electric conductivity, $\sigma_{\text{ice}}$ [S m <sup>-1</sup> ]	10 <sup>-5</sup> ‡		
Glacier basement			
<b>Porosity, <math>\phi</math></b>	(0.3)	<b>Water mass density, <math>\rho_w</math></b> [kg m <sup>-3</sup> ]	1000
Cementation exponent, $\hat{m}$	1.35	<b>Water viscosity, <math>\eta_w</math></b> [Pa s]	1.7 × 10 <sup>-3</sup>
Mass density of the solid grains, $\rho_s$ [kg m <sup>-3</sup> ]	2600	<b>Salinity, <math>C_0</math></b> [Mol/l]	(5 × 10 <sup>-3</sup> )
<b>Permeability, <math>\kappa</math></b> [m <sup>2</sup> ]	(2.11 × 10 <sup>-12</sup> )	<b>Permittivity of water, <math>\epsilon_w</math></b> [F m <sup>-1</sup> ]	85 $\epsilon_0$
<b>Matrix shear modulus, <math>G_b</math></b> [Pa]	(4.77 × 10 <sup>8</sup> )	<b>Temperature, <math>T</math></b> [K]	273
<b>Top depth, <math>z_b</math></b> [m]	(200)		

*Note:* Those not shown in this table can be obtained from them using the formulas given or referenced in this work. Parameters displayed in boldface are the inversion study free ones, their constant values between round brackets – referred to as ‘true values’ – are the ones used to compute the noiseless synthetic field data. Note that, as explained in Section 3, the true values for  $\kappa$  and  $G_b$  are computed in terms of  $\phi$  from rock physics models. Values marked with a \* symbol are taken from Collins, Frank and Metzler (2016), those marked with a ‡ symbol are given in Petrenko and Whitworth (1999). The vacuum permittivity is taken to be  $\epsilon_0 = 8.85 \times 10^{-12} \text{Fm}^{-1}$ .

We turn now the attention to the non-free parameters of the model. For the basement electric conductivity  $\sigma_b$ , we used Archie’s law (Archie 1942; Mavko, Mukerji and Dvorkin 2009)

$$\sigma_b = \frac{\sigma_w}{F}, \quad (9)$$

where  $\sigma_w$  is the electric conductivity of the saturating water in the glacier basement, and  $F = \phi^{-\hat{m}}$  is the formation factor, which expresses the reduction of the water conductivity due to the presence of the electrically insulating rock matrix. As described in Monachesi *et al.* (2018b), for water containing just dissolved NaCl, we can use  $\sigma_w = \sum_{l=\text{Na}^+, \text{Cl}^-} (ez_l)^2 b_l N_l$ , where  $e = 1.6 \times 10^{-19}$  C is the electron electric charge, and  $z_l$  is the ions’ valence; we used  $z_l = 1$  for both species. The ions’ mobility  $b_l$  and concentration  $N_l$ , both dependent on the salinity  $C_0$ , are calculated following Carcione, Seriani and Gei (2003). Note that the way in which we compute the bulk electric conductivity implies that the basement rock matrix is assumed to be clean, that is it does not contain a significant amount of clay. Had we considered otherwise, we would have used a corrected version, including the surface conductivity (Schön 1996), for which several models exist (a couple of them are discussed in Zyserman *et al.* 2017b).

To finish, we analyse the electrokinetic coupling coefficient  $L_0$  in equation (8), which depends on the non-free parameters  $\zeta$ ,  $d$  and  $\Lambda$ . We follow Pride (1994) and Santos (2009) for the treatment of their dependence on the free model parameters. For the  $\zeta$  potential, we use

$$\zeta = (0.008 + 0.26 \log_{10}(C_0)) \left( \frac{pH - 5}{2} \right). \quad (10)$$

In this work,  $pH = 7$  is employed. The parameter  $d$ , as we mentioned above, is the Debye length, computed as

$$d^{-1} = \sqrt{\sum_{l=\text{Na}^+, \text{Cl}^-} \frac{N_l (ez_l)^2}{\epsilon_w k T}}. \quad (11)$$

Here  $k = 1.3807 \times 10^{-23}$  J/K is the Boltzmann’s constant and  $T$  is the temperature; we use for  $z_l$  and  $N_l$  the same values as for the water conductivity  $\sigma_b$ . Finally, the parameter  $\Lambda$ , which can be seen as a pore surface to volume ratio (Johnson, Koplik and Dashen 1987; Pride 1994) is computed as

$$\Lambda = 2\sqrt{F\kappa}. \quad (12)$$

#### 4 COMPUTATION OF THE SYNTHETIC DATA

The values of the model parameters used to compute the synthetic data are listed in Table 1. Those not shown in the table can be obtained from them using the formulas given or referenced above. Of course, at this stage we also need to choose values for the free parameters, that is the ones we use in next sections in the inversion study. The chosen values are referred to as the ‘true values’ and they are displayed between round brackets. Note that when computing the synthetic data we decided, instead of assigning arbitrary values to the basement permeability  $\kappa$  and shear modulus  $G_b$ , to use a rock physics model to obtain them. For the estimation of the basement solid matrix shear modulus  $G_b$ , we use Walton’s model (Mavko *et al.* 2009), appropriate to model unconsolidated

media (Pride 2005; Bordes *et al.* 2015; Dupuy, Garambois and Virieux 2016):

$$G_b = \frac{1}{10} \left[ \frac{3(1-\phi)^2 \hat{C}^2 P}{\pi B^2} \right], \text{ with } B = \frac{1}{4\pi} \left( \frac{1}{G_s} + \frac{1}{G_s + \lambda_c} \right). \quad (13)$$

In this equation,  $\hat{C}$  is the coordination number, related to the packing of the spheres building the solid aggregate,  $P$  is the hydrostatic pressure and  $\lambda_c$  is Lamé's coefficient of the effective grain material, and is computed as  $\lambda_c = K_s - \frac{2}{3}G_s$ , where  $K_s$  is the bulk modulus of the solid grains. In this work, we consider  $\hat{C} = 9$ . The hydrostatic pressure can be computed as  $P = P_0 + \rho_{\text{ice}} g z_b$ , being  $P_0 = 101,325$  Pa the air pressure at the surface of the Earth and  $g = 9.81 \text{ m s}^{-2}$  the gravity of Earth. Taking  $G_s = 45$  GPa and  $K_s = 36$  GPa representative for the shear and bulk moduli of quartz grains, respectively (Mavko *et al.* 2009), we obtain, as displayed in Table 1,  $G_b = 0.477$  GPa. To compute the value for the basement permeability to be employed in the computation of the synthetic field data, we use (Mavko *et al.* 2009)

$$\kappa = \frac{1}{72} \left( \frac{D_q}{\phi F} \right)^2 \frac{\phi^3}{(1-\phi)^2}; \quad (14)$$

in this model, referred to as Kozeny–Carman equation,  $D_q = 8 \times 10^{-5}$  m is the diameter of the quartz grains. Using  $\phi = 0.3$ , one obtains  $\kappa = 2.11 \times 10^{-12} \text{ m}^2$ , as displayed in Table 1.

Having all the model parameters set, we can turn our attention to the shear horizontal seismic source and the simulation of noisy data. To calculate the time signature of the source  $F^s(t)$ , we use a Ricker wavelet with peak frequency  $f_{\text{peak}} = 120$  Hz; its peak amplitude, located at  $t = 8 \times 10^{-3}$  s, is set so that the maximum amplitude of the force per unit area at the surface is  $1 \text{ N m}^{-2}$ . Monachesi *et al.* (2018b) followed previous studies of shear wave sources (Bordes 2005; Krawczyk *et al.* 2013) to compute a source amplitude close to actual field values. In that case, the aim was to test the feasibility of the seismoelectric method by estimating the minimum amplitude that would be recorded at the surface, for which a realistic amplitude value is crucial. In the present study, we focus on testing the feasibility of retrieving the model parameters from the data. We set a recording time of 1.024 seconds, and Fourier transform the source using a sampling period of  $0.5 \times 10^{-3}$  s to take  $N_t = 2048$  samples in the frequency domain. The seismic and electromagnetic responses are computed in the frequency domain, and inverse Fourier transformed to recover them back in the time domain (see the Appendix). The number of samples is chosen as a power of 2 in order to efficiently employ the fast Fourier transform

when going to the frequency domain and its inverse to move backwards to the time domain. In Fig. 2, we show the time signature of the source, and the computed time traces for solid displacement and electric field at the surface. We set  $z = 0$  and for each frequency, we use equation (A1) to get  $u_x(0)$  and equation (A6) to get  $E_x(0)$ . Afterwards, we inverse Fourier transform them and obtain the traces displayed in the figure. We do not employ the magnetic field in the inversion because, as stated in Monachesi *et al.* (2018b), its amplitude at the surface is very small compared to its amplitude below the glacier basement, and thus very difficult to be measured.

The synthetic data  $\mathbf{d} = (\mathbf{d}_E, \mathbf{d}_S)$  are computed according to the following expressions

$$d_{E,i} = (1 + p_E r_i) \hat{d}_{E,i}, \quad (15)$$

$$d_{S,i} = \hat{d}_{S,i} + p_S r_i. \quad (16)$$

In this equations,  $\hat{d}_{E,i}$  is the  $i$ th sample of the time series that represents the noise-free computed electric field and  $\hat{d}_{S,i}$  the corresponding sample for the noise-free computed solid displacements.  $r_i$  is the  $i$ th sample of an  $N_t$ -dimension random noise time series following a zero mean normal distribution, while  $p_E$  and  $p_S$  are positive factors controlling the amplitude of the noise we want to add to the noiseless electric and seismic signals, respectively. Note that the noise added to the electric and seismic noise-free data,  $n_{E,i}$  and  $n_{S,i}$ , are different. For the electric case, we assume  $n_{E,i} = p_E r_i \hat{d}_{E,i}$ , that is, the noise is proportional to the signal so its amplitude is controlled by  $\hat{d}_{E,i}$  and  $p_E$ , whereas for the seismic case  $n_{S,i} = p_S r_i$ , that is, the noise is independent from the signal (Chen *et al.* 2007). The way the error term is generated for each type of field follows their own standards. In the seismic case, one way to quantify the noise level is by means of the signal-to-noise ratio (SNR) (Robinson and Treitel 2000) which can be defined as the ratio of the squared  $l_2$ -norms of the clean data and the noise, that is,

$$\text{SNR} = \frac{\|\hat{\mathbf{d}}_S\|_2^2}{\|\mathbf{n}_S\|_2^2} = \frac{\|\hat{\mathbf{d}}_S\|_2^2}{p_S^2 \|\hat{\mathbf{r}}\|_2^2}, \quad (17)$$

which means that  $p_S$  can be chosen to yield a predefined value for SNR. In the electric case, synthetic data are generated adding to the noiseless data a percentage of such signal multiplied by a random noise series (Kalscheuer *et al.* 2010; Rosas-Carbalajal *et al.* 2014). The noise term corresponding to both electric and seismic signals can be thought as the error of the measurements simulated by the synthetic data set. Given the way these are calculated, the errors result to be uncorrelated. The way the noise is constructed allows us to tune

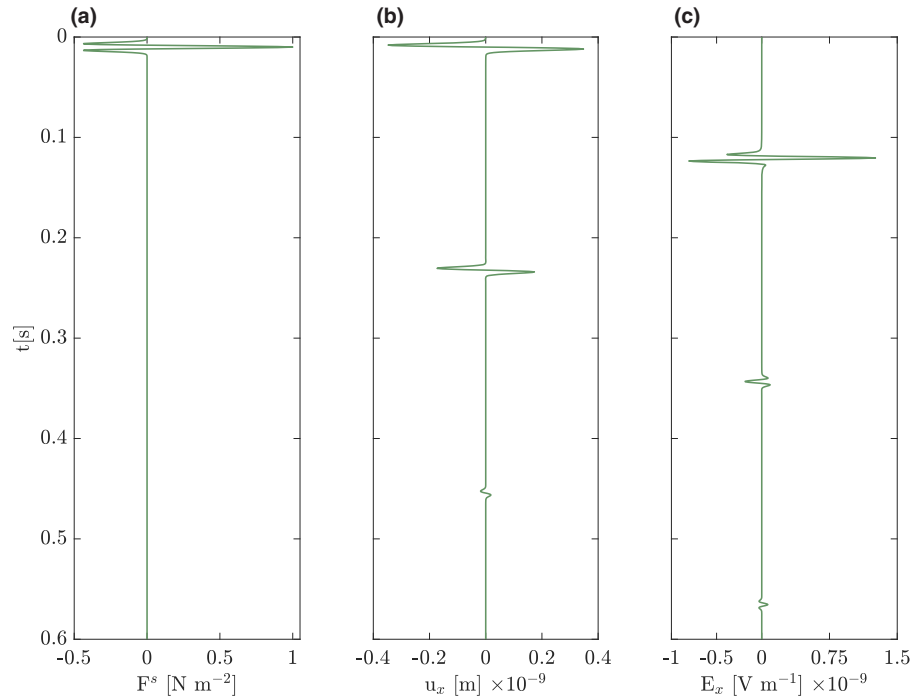


**Figure 2** (a) Time signature of the shearing force  $F^s(t)$  employed as source, (b) the solid displacement  $u_x(t)$  and (c) the electric field response  $E_x(t)$ , both computed at the surface (b and c show the noise-free time series to which various levels of noise were added prior to inversion).

different errors in terms of SNR and percentage of noiseless signal for the seismic and electric case, respectively, so that we are able to obtain synthetic data that permits to accomplish our feasibility study.

## 5 BAYESIAN INFERENCE OF RELEVANT MODEL PARAMETERS

The resolution of the inverse problem aims at determining the model parameters presented before, together with their uncertainties. Following a probabilistic approach implies that, instead of searching an exact model, we intend to characterize the full posterior probability density function (pdf) of the model parameters. This function is related to the previous knowledge about the model, and to the pdf of the data set given a certain model, through Bayes' theorem:

$$p(\mathbf{m}|\mathbf{d}) = \frac{p(\mathbf{m})p(\mathbf{d}|\mathbf{m})}{p(\mathbf{d})}, \quad (18)$$

where  $p(\mathbf{m}|\mathbf{d})$  is the posterior pdf of the model parameters conditioned on the data set;  $p(\mathbf{m})$  is the prior pdf, which accounts for the *a priori* information of the model parameters;  $p(\mathbf{d}|\mathbf{m})$  is the probability of the data conditioned on the model parameters, which also appears in the literature as the likelihood function; and  $p(\mathbf{d})$  is the pdf of the data, also known as

evidence, which is constant for a fixed model parametrization. As the present work involves such type of parametrization, we can dismiss the evidence and, instead of using the equality in equation (18), we employ a proportional relationship to obtain the posterior pdf:

$$p(\mathbf{m}|\mathbf{d}) \propto p(\mathbf{m})p(\mathbf{d}|\mathbf{m}). \quad (19)$$

Whenever possible,  $p(\mathbf{m}|\mathbf{d})$  should be obtained by providing explicit expressions for  $p(\mathbf{d}|\mathbf{m})$  and  $p(\mathbf{m})$ . In practice, this is rarely possible, especially for calculating  $p(\mathbf{d}|\mathbf{m})$ , which often implies the use of numerical methods to solve the forward problem. We thus have to resort to numerical methods, which may allow us to retrieve the marginal pdf of each separate parameter of interest instead of the complete posterior distribution  $p(\mathbf{m}|\mathbf{d})$ , or effectively sample the parameter space to obtain a collection of models which follows  $p(\mathbf{m}|\mathbf{d})$ . In the following, we describe each of these strategies.

### 5.1 Marginal distributions via numerical integration

As a first approach to characterize the uncertainty of the model parameters  $\mathbf{m}$  in a Bayesian framework, we attempt to calculate their marginal posterior distributions. Following Brandt (1989), let  $f(\mathbf{m})$  be the joint probability density of  $M$  variables



$\mathbf{m} = (m_1, m_2, \dots, m_M)$ . The marginal distribution of a single parameter  $m_r$  is given by

$$g_r(m_r) = \int_{-\infty}^{\infty} \int_{-\infty}^{\infty} \dots \int_{-\infty}^{\infty} f(\mathbf{m}) dm_1 dm_2 \dots dm_{r-1} dm_{r+1} \dots dm_M \quad (20)$$

and it can be interpreted as the probability density of  $m_r$ , accounting for the uncertainty of the remaining model parameters. Then the marginal distribution  $g_r(m_r)$  can be used to compute the mean  $\mu_r$  and variance  $\sigma_r^2$  of  $m_r$  as

$$\mu_r = \int_{-\infty}^{\infty} m_r g_r(m_r) dm_r, \quad \sigma_r^2 = \int_{-\infty}^{\infty} (m_r - \mu_r)^2 g_r(m_r) dm_r. \quad (21)$$

In our case, the vector of model parameters, which refers to the glacier depth and basement properties, is characterized as follows:

$$\mathbf{m} = (\phi, z_b, G_b, \kappa, C_0). \quad (22)$$

Instead of working with the proper values for the bulk modulus, the permeability and the salinity, the inversion and the previous sensitivity analysis are performed in  $\log_{10}$  scale. This is because these parameters present order-of-magnitude variations in nature, and so it is more reasonable to explore the space of model parameters using a  $\log_{10}$  scale (Tarantola 2005). Regarding the parameters that are sampled in  $\log_{10}$  scale, it is worth to mention that each one of them has dimensions and the units of each magnitude are accordingly indicated.

We assume a Gaussian behaviour of the data errors and uniform prior distributions for the model parameters (i.e. Jeffreys priors for  $\log_{10}$  variables, Tarantola 2005). The Gaussian behaviour of the data means that  $p(\mathbf{d}|\mathbf{m})$  in equation (19) corresponds to an exponential function whose argument contains the difference between the data and the response predicted by the model. A uniform prior implies that, for each parameter  $m_r$ , all the values lying in the chosen interval have the same probability. Under these hypotheses for the model parameters and the data and following equation (19),  $p(\mathbf{m}|\mathbf{d})$  has the form:

$$p(\mathbf{m}|\mathbf{d}) = V \exp\left(-\frac{\Phi}{2}\right), \quad (23)$$

where  $V$  is a normalization factor and  $\Phi$  is the data misfit, whose explicit form will be given in Section 6.2.

In this way, if we consider for example the porosity, its marginal distribution can be obtained according to equation (21) as

$$g_\phi(\phi) = \int_{z_{b,\min}}^{z_{b,\max}} \int_{G_{b,\min}}^{G_{b,\max}} \int_{\kappa_{\min}}^{\kappa_{\max}} \int_{C_{0,\min}}^{C_{0,\max}} p(\mathbf{m}|\mathbf{d}) dz_b dG_b d\kappa dC_0, \quad (24)$$

where the minimum and maximum values of the integrals result from the non-zero limits of the corresponding prior distributions. Note that we can compute the coefficient  $V$  appearing in equation (23) by employing the condition that the integration of  $p(\mathbf{m}|\mathbf{d})$  over the whole parametric space is equal to 1. Therefore,

$$V^{-1} = \int_{\phi_{\min}}^{\phi_{\max}} \int_{z_{b,\min}}^{z_{b,\max}} \int_{G_{b,\min}}^{G_{b,\max}} \int_{\kappa_{\min}}^{\kappa_{\max}} \int_{C_{0,\min}}^{C_{0,\max}} \exp\left(-\frac{\Phi}{2}\right) dz_b dG_b d\kappa dC_0 d\phi, \quad (25)$$

and the mean value and variance are given by

$$\mu_\phi = V^{-1} \int_{\phi_{\min}}^{\phi_{\max}} \phi g_\phi(\phi) d\phi, \quad \sigma_\phi^2 = V^{-1} \int_{\phi_{\min}}^{\phi_{\max}} (\phi - \mu_\phi)^2 g_\phi(\phi) d\phi. \quad (26)$$

The mean values and variances of the other model parameters are obtained in the same way.

To accomplish this task, we resort to multidimensional numerical integration, which is not easy to implement (Press *et al.* 2007). A straightforward generalization of one-dimensional numerical integration leads to very long computing times even for integrals in low dimensions as the ones we are dealing with. We therefore employ the multidimensional integration library Cuba (Hahn 2005), which offers four different approximation methods to compute the integrals. We tested all of them, and because of its better performance we decided to work with the Divonne routine.

## 5.2 MCMC inversion

Analytical solutions to equation (18) are seldom possible. Markov chain Monte Carlo (MCMC) algorithms can be used to sample the posterior probability density function (pdf) by searching through the parameter space (Tarantola and Valette 1982; Mosegaard and Tarantola 1995; Sambdrige and Mosegaard 2002; Ter Braak 2006; Vrugt *et al.* 2009; Rosas-Carbajal *et al.* 2015). Monte Carlo methods draw samples of the desired distribution and Markov chains guide properly this sampling in an efficient manner. Under certain conditions, Markov chains become independent from the initial state and, after a *burn-in* period, they converge to its stationary distribution (Gilks, Richardson and Spiegelhalter 1995). Therefore, we have to construct a Markov chain such that its stationary distribution is the one we are seeking. There

are many ways to accomplish this task, but in general the Metropolis–Hastings algorithm is used. Briefly, given the current state of the chain  $\mathbf{m}_t$ , a candidate point  $\mathbf{m}^*$  is drawn from a proposal distribution which then is accepted with probability  $\alpha$ :

$$\alpha(\mathbf{m}_t|\mathbf{m}^*) = \min \left\{ 1, \frac{\pi(\mathbf{m}^*)q(\mathbf{m}_t|\mathbf{m}^*)}{\pi(\mathbf{m}_t)q(\mathbf{m}^*|\mathbf{m}_t)} \right\}, \quad (27)$$

where  $\pi(\cdot)$  is the target distribution and  $q(\cdot)$  is the proposal distribution. If the candidate point is accepted, then  $\mathbf{m}_{t+1} = \mathbf{m}^*$ . Otherwise, the chain remains in the current state (Gilks *et al.* 1995). We employ an Adaptive Metropolis scheme, in which the proposal distribution is updated according to the samples that are continuously drawn from the posterior (Hassan, Bekhit and Chapman 2009). This scheme, after a certain amount of iterations, will produce samples that follow the posterior distribution we are looking for. As we are using uniform priors, the acceptance rule can be calculated in terms of the ratio of the likelihoods of two states (Mosegaard and Tarantola 1995).

The MCMC algorithm is implemented through the Differeential Evolution Adaptive Metropolis algorithm (Vrugt *et al.* 2009), which efficiently copes with non-linear problems. A remarkable feature of this algorithm is that it uses several Markov chains in parallel to converge to the target distribution. The information recovered by the chains is mixed using a formulation that incorporates properties of genetic algorithms. The following equation describes such behaviour:

$$\mathbf{z}^i = \mathbf{x}_{t-1}^i + \gamma (\mathbf{X}_{t-1}^{r_1} - \mathbf{X}_{t-1}^{r_2}) + \epsilon, \quad r_1 \neq r_2 \neq i, \quad (28)$$

where  $\mathbf{z}^i$  is a sample of the  $i$ th chain, which combines a sample of the previous iteration of the same chain  $\mathbf{x}_{t-1}^i$  with a linear combination of members of the rest of the chains  $\mathbf{X}_{t-1}^{r_1}$ . The constant  $\gamma$  sets the jump rate with which the chains sample different regions of the parameter space. This allows to automatically tune the scale and orientation of the proposal distribution.  $\epsilon$  is the perturbation of ergodicity, which controls how much a state of the chain depends on the previous one. The choice of the different values follows the criterion stated in Vrugt *et al.* (2009), where the optimal value is given by the expression  $\gamma = 2.38/\sqrt{2\delta}$ , where  $\delta$  is the dimensionality of the problem, which refers to the number of parameters desired to be constrained in the inversion. This quotient comes from the properties of Random Walk Metropolis and this factor is appropriate for Gaussian distributions. Finally, the convergence of the chains to the target distribution is expected to be reached when the Gelman–Rubin factor ( $\hat{R}$ ) is less than 1.2 (Gelman and Rubin 1992).

## 6 RESULTS

We start by briefly describing the synthetic seismic and electric signals produced or electrokinetically induced, respectively, by the seismic source. We follow by studying the sensitivity of the data to the model parameters and we end this section by analysing the outcome of the chosen inversion methods.

### 6.1 Forward model: seismic and electric data

The time signature of the noiseless solid displacement computed at the surface (Fig. 2) exhibits four events evenly spaced in time; three of them are clearly observable in the figure and the last one is a tiny hump. The first signal arrives at the very moment the source energy is released, because it corresponds to the direct wave. A second arrival occurs 0.22 seconds after the detonation of the source. This is the time needed by the wave in its way forth and back between the surface and the glacier-basement interface (the velocity of the seismic wave is 1800 m/s and  $z_b = 200$  m), corresponding to a first reflection at the interface. The third event arrives at twice the time of the second one, corresponding to a second reflection at the glacier-basement interface. Finally, the fourth arrival is recorded at a time 0.66 seconds, and corresponds to a third reflection. Note that the amplitudes of the consecutive events are diminishing with time. This is because when the wave hits the interface, part of its energy is released to the basement as a transmitted wave, while the remaining energy travels back to the surface as a reflected wave. The amplitudes of both reflected and transmitted waves at the  $n$ th incidence at  $z = z_b$  are given by equations (A2) and (A4), respectively (see the Appendix).

Turning now the attention to the electric field (Fig. 2c), it can be noticed that three events are recorded within the considered time window. The first one arrives at 0.11 seconds, which is half the arrival time of the second seismic event. This recorded arrival is due to an interface response (IR) produced when the seismic wave hits the interface. As it was studied in Monachesi *et al.* (2018b), the source of this IR is the jump in the electric current density occurring at the interface between the glacier and its basement (the current density is zero at the ice because of the absence of fluids, and is different from zero at the glacier basement). Once the seismic wave hits the interface, the produced IR travels to the surface at a speed given by  $\sqrt{2\omega}/(\mu_0\sigma)$ ; this is approximately  $10^5$  m/s at the source peak frequency, much higher than that of the seismic wave. This explains why the observed arrival time for the first event is half the time of the first seismic arrival.

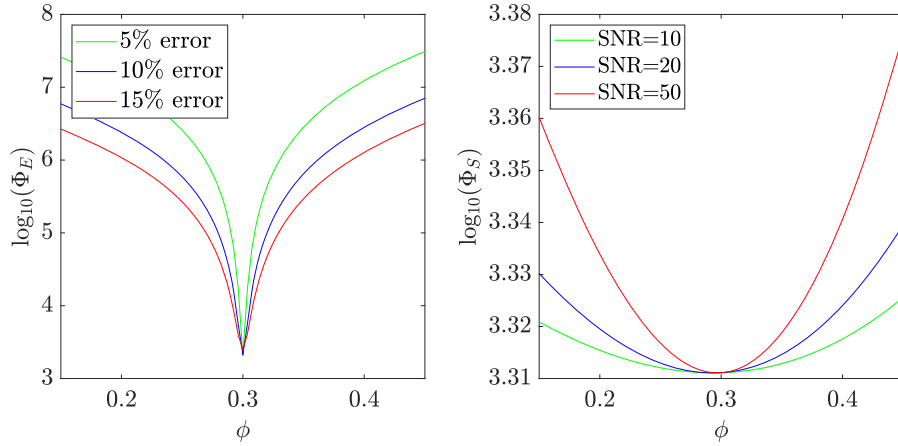


**Figure 3** Misfits computed as a function of the porosity  $\phi$ . (a) The electric contribution to the total misfit, for three percentages of error in the electric data. (b) The seismic misfits due to three signal-to-noise ratios in the seismic data. Both the seismic and electric traces comprise all time samples,  $N_t = 2048$ .

Regarding the second and third events, it is now clear from simple inspection of Figure 2 that they, respectively, correspond to IRs produced by the second and third incidences of the seismic wave over the interface. Note that as in the case of the solid displacement, the electric field shows an amplitude decay for the consecutive events. This is because the amplitude of the electric field is proportional to the amplitude of the electric current density (see equations (A6) and (A10)) which in turn is proportional to the amplitude of the solid displacement.

## 6.2 Sensitivity analysis in terms of data misfits

To evaluate the possibility of retrieving the relevant model parameters through data inversion, we study their influence on the seismic and electric data misfits. We choose an  $l_2$ -norm measure for the electric field and solid displacements data misfits, which is adequate for Gaussian errors (Rosas-Carbajal *et al.* 2014, 2015). The seismic and electric misfits are

$$\Phi_E = \sum_{i=1}^{N_t} \left( \frac{d_{E,i} - \hat{d}_{E,i}}{p_E d_{E,i}} \right)^2, \quad \Phi_S = \sum_{i=1}^{N_t} \left( \frac{d_{S,i} - \hat{d}_{S,i}}{p_S} \right)^2, \quad (29)$$

respectively. The denominators in  $\Phi_E$  ( $\Phi_S$ ) are their corresponding standard deviations of the  $i$ th electric field (solid displacements) errors. The misfit for the joint problem is

$$\Phi = \Phi_E + \Phi_S, \quad (30)$$

which is replaced in equation (23) to calculate  $p(\mathbf{m}|\mathbf{d})$ . To study the sensitivity of each relevant parameter, we calculate the misfit between the synthetic data and the for-

ward model response computed using the true model parameters, except for the parameter chosen to perform the analysis.

First of all, we evaluate how many events are appropriate to be considered in the sensitivity analysis and consequently in the inversion study. It is clear that  $n$  cannot be higher than 3, because the third event has already a very small amplitude (Fig. 2b). Moreover, the seismic and electric traces with  $n = 1$  have already all the physical information we want to recover. However, increasing the number of events provides a larger data set, which from a statistical point of view reinforces the probabilistic approach, according to the law of large numbers (Jeffreys 1998). This is why we choose to use the traces with three events, which leads to a data set of  $N = 2N_t = 4096$ .

We now determine through a misfit analysis whether the seismic and electric data are sensitive or not to changes in the model parameters. We perform this study by varying each one of them at a time over a predefined prior domain, while leaving the others fixed and equal to the true values. The best scenario is that the log-misfits exhibit a clear and sharp minimum around the true value for each parameter. For the electric data, we employed three percentages of error to corrupt the true model response: 5%, 10% and 15%. In the seismic case, we generated synthetic data sets using  $\text{SNR} = 10, 20$  and 50. The electric misfit exhibits a sharp minimum near the true value for the porosity parameter, whereas the seismic data misfits present smooth minima near the true value of porosity for the three signal-to-ratio (SNR) cases (Fig. 3). Both the electric and seismic misfit show a sharp minimum near the true value of the depth (Fig. 4), though the curves differ

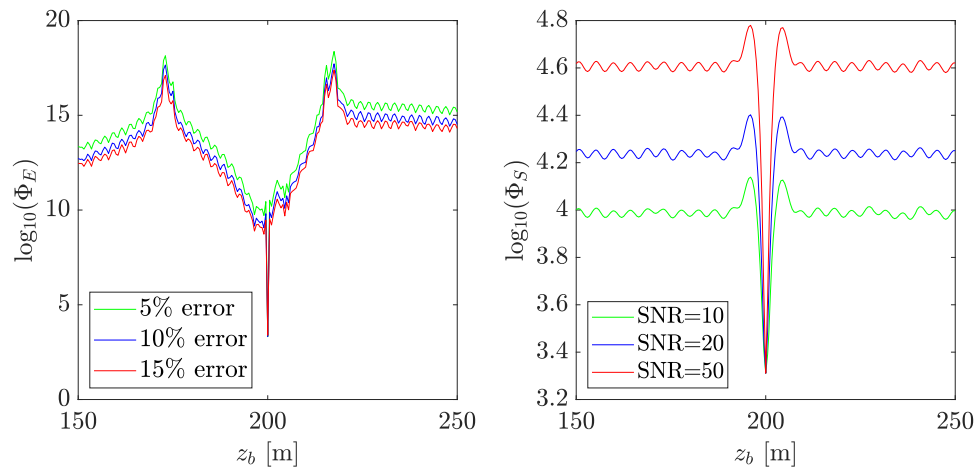


**Figure 4** Misfits computed as a function of the depth of the top of the basement  $z_b$ . (a) The electric contribution to the total misfit, for three percentages of error in the electric data. (b) The seismic misfits due to three signal-to-noise ratios in the seismic data. Both the seismic and electric traces comprise all time samples,  $N_t = 2048$ .

considerably from the behaviour as a function of the porosity, presenting an oscillatory behaviour. The electric and seismic misfits also present sharp minima as a function of the shear modulus in all cases (Fig. 5). The seismic case minima are a little bit smoother than the electric ones, but are still very distinctive. The electric misfit show sharp minima near the true value of the permeability, while the seismic misfit remain constant for permeabilities lower than  $10^{-10} \text{ m}^2$  (Fig. 6). This fact is correlated with the results of the inversion of seismic data (Section 6.4). Finally, the misfit analysis of the salinity is only referred to the electric data because the physics of the problem do not relate the seismic response to this parameter. There are

also sharp minima near the true value of the concentration (Fig. 7).

We can conclude that the synthetic data are sensitive to the whole parameter set. In general, the misfits become larger for the lowest percentage of error in the electric data and the highest SNR in the seismic data (both cases represent the less realistic synthetics). This fact is key for the election of the synthetic set for the inversion, because the numerical computation of the marginal distributions has problems dealing with large misfits. We select the electric data with an error of 10% of the amplitude of the response of the true model and the seismic data with an  $\text{SNR} = 20$ .

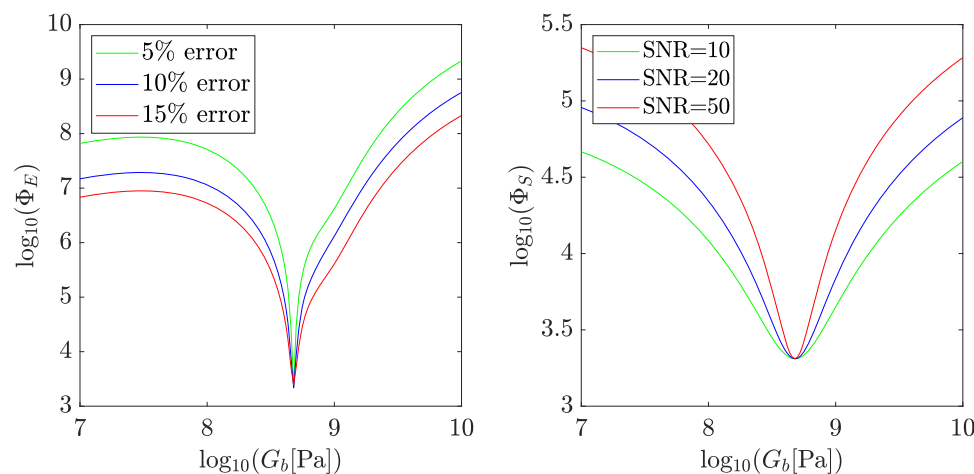


**Figure 5** Misfits computed as a function of the basement rock matrix shear modulus  $G_b$ . (a) The electric contribution to the total misfit, for three percentages of error in the electric data. (b) The seismic misfits due to three signal-to-noise ratios in the seismic data. Both the seismic and electric traces comprise all time samples,  $N_t = 2048$ .

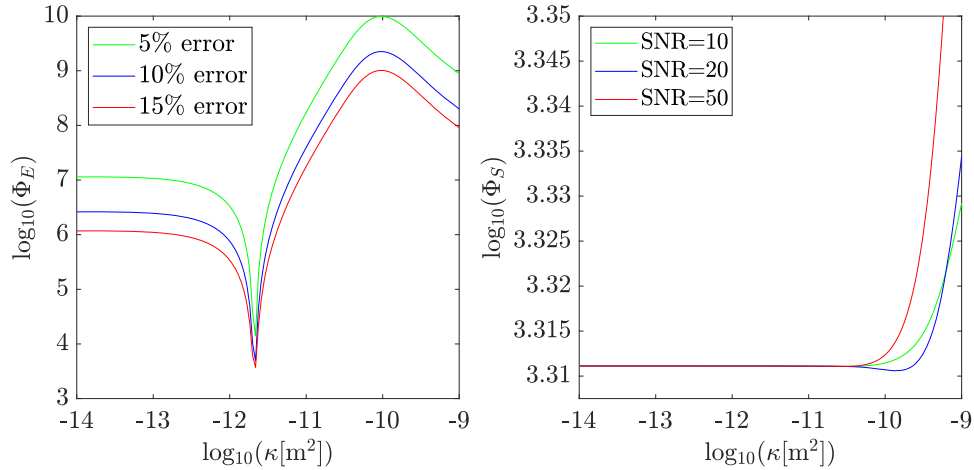


**Figure 6** Misfits computed as a function of the permeability  $\kappa$ . (a) The electric contribution to the total misfit, for three percentages of error in the electric data. (b) The seismic misfits due to three signal-to-noise ratios in the seismic data. Both the seismic and electric traces comprise all time samples,  $N_t = 2048$ .

### 6.3 Multidimensional numerical integration

We first attempt to obtain the posterior marginal distribution of each model parameter by integration, and from them the resulting means and standard deviations. The computation of the marginal probability density functions (pdfs) (see equation (24) for the porosity case) is a numerically challenging task, even with a dedicated software as the one we employ.

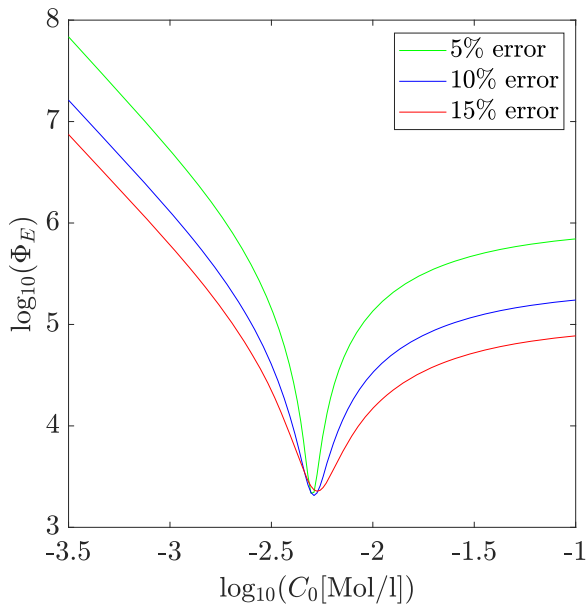


**Figure 7** Electric misfit computed as a function of the water salinity, for three percentages of error in the electric data. We do not display the seismic misfits, because they are just constants, as expected. The electric trace comprises all time samples,  $N_t = 2048$ .

Due to the large values of the misfit  $\Phi$ , the computation has to be performed in quadruple precision in order to avoid the integrand to be identically zero. Indeed, as the minimum misfit value is  $\Phi = 4096$ , the highest value the integrand of the marginal pdfs can take is  $\exp(-2048)$ , that is, approximately  $3.7 \times 10^{-890}$ , a much lower value than the inferior limit the double precision allows to represent. Furthermore, a simple inspection of Figs 3–7 shows that the misfit takes values higher than  $10^4$  but for a small interval enclosing the true values. We mention this because beyond this value the integrand is taken as zero, even in quadruple precision. Thus, in order to be able to compute the marginal pdfs, that is, the numerical algorithm performs an appropriate sampling near the true values, we were forced to restrict the integration limits to rather small intervals around them, which is equivalent to considering small prior pdf ranges for  $p(\mathbf{m})$ .

Having clarified this point, we show in Fig. 8 the obtained posterior marginal pdfs of the model parameters. They were obtained following a procedure that we here describe for the porosity, but is similar for the whole parameter set. The calculations follow this scheme: we choose 20 porosity values equally distributed among the prior limits. We compute the integral given in equation (24), that is a four-dimensional integral, using the Divonne routine from the Cuba library. Afterwards, we estimate the reciprocal of the normalization factor  $V$ , by simply applying a one-dimensional Simpson's rule using the obtained discrete marginal distribution values as ordinates, and the chosen values as abscissae. This result is used to normalize the set of calculated  $g_\phi(\phi_i)$ ,  $i = 1, \dots, 20$ , which we display in Fig. 8a. Finally, the mean value  $\mu_\phi$

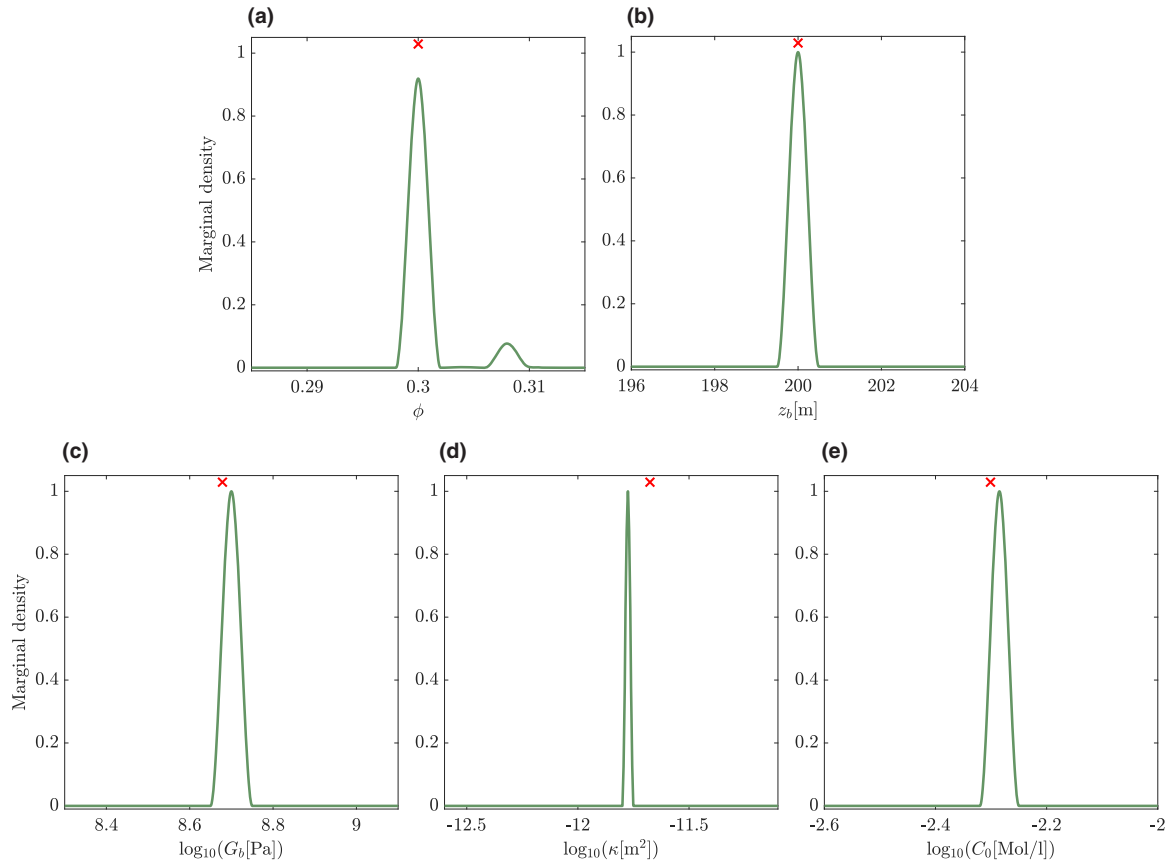


**Figure 8** Marginal pdf, computed following the procedure described in Section 6.3 for (a) porosity, (b) glacier depth  $z_b$ , (c)  $\log_{10}$  of basement shear modulus, (d)  $\log_{10}$  of permeability and (e)  $\log_{10}$  of saturating water salinity. Note that the considered integration intervals are:  $[\cdot 28, \cdot 32]$  for  $\phi$ ,  $[195, 205]$  for  $z_b$ ,  $[8.2, 9.2]$  for  $\log_{10}(G_b)$ ,  $[-12.2, -11.3]$  for  $\log_{10}(\kappa)$  and  $[-2.6, -1.9]$  for  $\log_{10}(C_0)$ .

and the variance  $\sigma_\phi^2$  (see equation (26)) are in turn computed by again applying Simpson’s rule in one dimension. In Table 2, we display the mean values and standard deviations obtained for all the model parameters. The results obtained by this methodology are, we deem, deceptively promising. The marginal distributions are very narrow and their peaks

are very close to the respective true values, which is reflected in the computed standard deviations. This is particularly true for  $z_b$ , for which just one value of  $g_{z_b}(z_{b,i}), i = 1, \dots, 20$  is not zero. However, these results are at least a consequence of having reduced the integration limits to small intervals around the true values. We consider that this fact alone is enough to

**Table 2** Mean value  $\mu$  and standard deviation  $\sigma$  for the five random variables considered, obtained by means of numerical computation of the integrals in equation (26) and using the DREAM algorithm. For the latter, we show values corresponding to single seismic inversion, single electromagnetic inversion and joint inversion [Correction added on 16 April 2020, after first online publication: there were previously errors in the layout of Table 2 and these have now been corrected in this version.]

Variables	True value	Numerical integration		DREAM		
		$\mu \pm \sigma$		Seismic Inversion	Electric Inversion	Joint Inversion
$\phi$	0.3	$0.3 \pm 8 \times 10^{-4}$		$0.29 \pm 0.093$	$0.31 \pm 0.046$	$0.3 \pm 0.038$
$z_b$ [m]	200	$200 \pm 0.0$		$200 \pm 0.004$	$200 \pm 0.0001$	$200 \pm 0.0001$
$\log_{10}(G_b[\text{Pa}])$	8.68	$8.7 \pm 3 \times 10^{-39}$		$8.67 \pm 0.031$	$8.68 \pm 0.015$	$8.68 \pm 0.012$
$\log_{10}(\kappa [\text{m}^2])$	-11.68	$11.78 \pm 5 \times 10^{-12}$		$-11.09 \pm 1.4$	$-11.67 \pm 0.09$	$-11.68 \pm 0.076$
$\log_{10}(C_0 [\text{Mol/l}])$	-2.3	$-2.29 \pm 2 \times 10^{-10}$		—	$-2.28 \pm 0.08$	$-2.295 \pm 0.072$

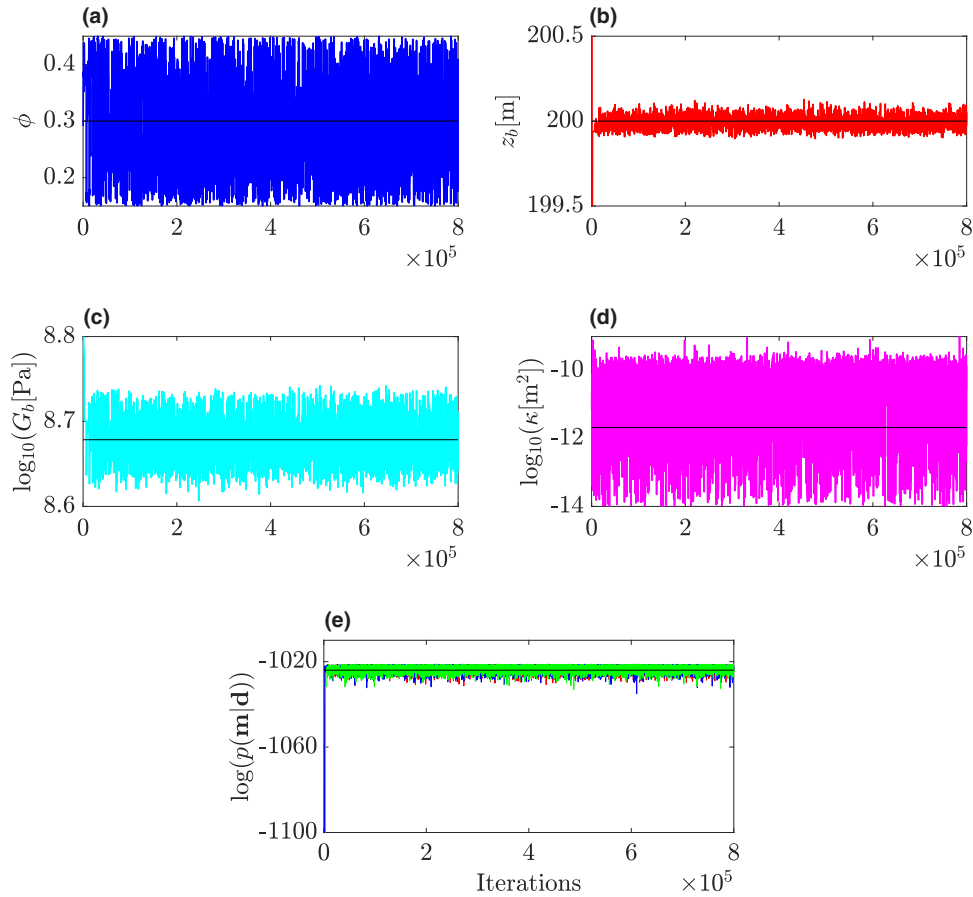


**Figure 9** A single chain represents the search through the prior of the porosity (a), the depth (b), the shear modulus (c) and the permeability (d) for the inversion of seismic data. (e) The convergence of  $\log(p(\mathbf{m}|\mathbf{d}))$  (for the three chains in colour blue, red and green) to the expected value  $-\mathcal{N}_t/2$ , denoted by the solid horizontal black line.

explore another methodology to characterize the model parameters uncertainty. In addition, the computational cost of the discussed numerical integration method is not low, because to compute each marginal at least  $10^6$  forward problem computations are needed.

#### 6.4 Inversion via the DREAM algorithm

We now evaluate the possibility of retrieving the full posterior probability density function (pdf) of the model parameters using the DiffereNtial Evolution Adaptive Metropolis algorithm. We perform the inversion of both seismic and electric data sets separately and jointly. For all cases, we use three parallel Markov chains, such that the model proposals of each chain are created accounting for the current state of the two others (see equation 28). The outcome of this process is a set of models that follow the posterior pdf. To represent this pdf, we display histograms of the last 50% of the chains states, once

convergence has been achieved. For all cases, we employed uniform priors:  $[0.15, 0.45]$  for  $\phi$ ,  $[150, 250]$  for  $z_b$ ,  $[6, 9]$  for  $\log_{10}(G_b)$ ,  $[-14, -9]$  for  $\log_{10}(\kappa)$  and  $[-4, -1]$  for  $\log_{10}(C_0)$ . The last parameter is only considered in the inversion of electric data and in the joint inversion of seismic and electric data, as referred in Section 6.2.

We first present the results concerning the inversion of seismic data alone. Figure 9a–d displays how the chains sample the parameter space (to clarify the curves, we only display a single chain but the behaviour is similar to the remaining two chains). The expected result is that the process of sampling eventually converges near the true value of each parameter. We tested different values of  $\gamma$ , around the optimal value of 0.85 (corresponding to  $\delta = 4$ , the number of parameters involved) in order to improve the exploration of the parameter space. In the case of  $\phi$ , the chains sample the complete model space defined by the prior distribution without converging to a smaller uncertainty range (Fig. 9a),

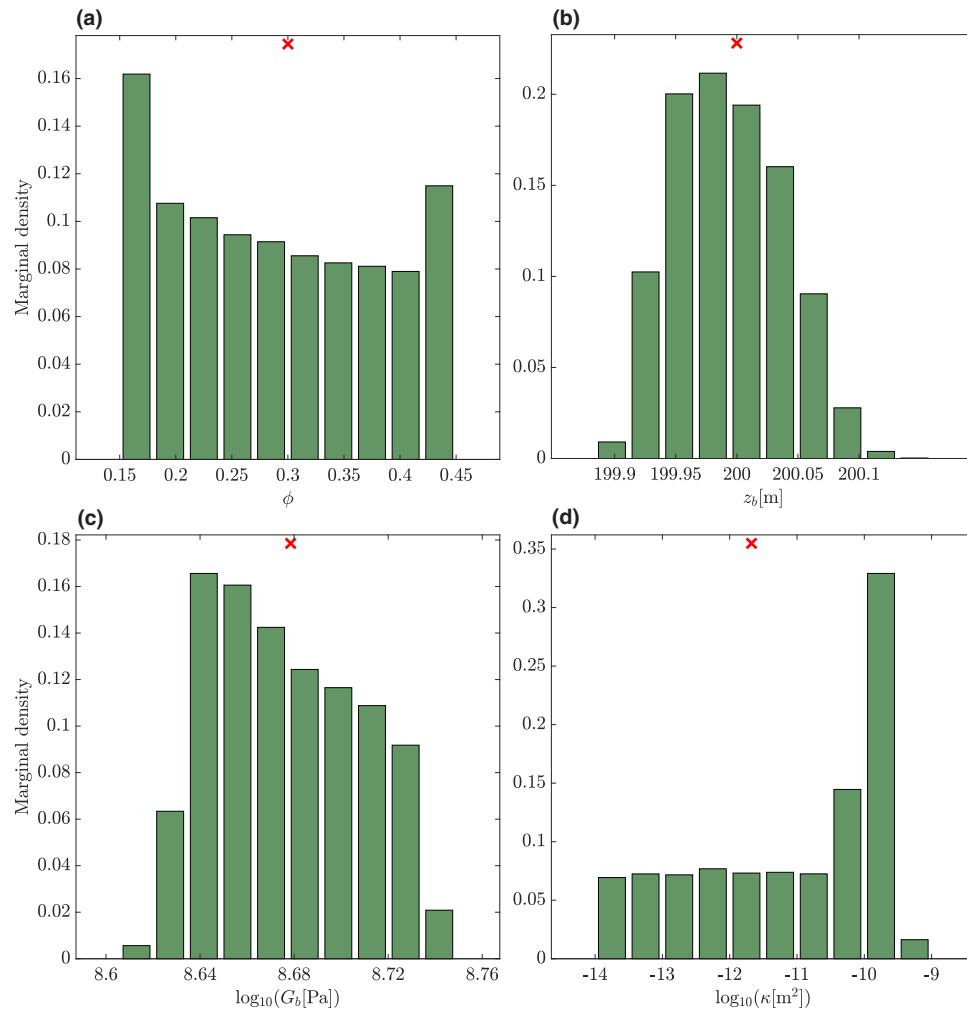


**Figure 10** Histograms of the basement porosity (a), the depth (b), the bulk modulus (c) and the permeability (d) for the inversion of seismic data. The red cross indicates the true value for each parameter.

despite the relatively high number of iterations employed ( $8 \times 10^5$  iterations). A straightforward convergence of the chains near the true value can be observed for  $z_b$  (Fig. 9b), and the path of the chains for  $G_b$  has a fairly similar behaviour (Fig. 9c), except that the chains oscillate around the true value in the end, but with a small amplitude. Finally, the behaviour of  $\kappa$  is similar to that of  $\phi$  (Fig. 9d), that is, the inversion of seismic data is not able to constrain this value further than the uniform prior pdf established. Besides collecting the sets of model parameters accepted, the algorithm stores the value of  $p(\mathbf{m}|\mathbf{d})$  of each accepted set of parameters (see equation 23). This value is expected to be approximately  $-N_i/2$  ( $-1024$  in this case) for models that reproduce statistically the data inverted. The chains indeed move around this value (Fig. 9e).

We evaluate the results of the inversion through histograms of the marginal distributions of the model parameters (Fig. 10). These histograms are built using the last 50% of the chains shown in Fig. 9, that is, only after the chains are considered to have converged according to the criteria by Gelman and Rubin (1992). In this way, histograms are representative of the marginal posterior pdf of each parameter, accounting for the uncertainty of all the other parameters considered (see equation 20).  $z_b$  and  $G_b$  are the best resolved parameters of this inversion (Figs 10a and d, respectively). Their histograms are rather bell-shaped, with peaks near the true model values. Unlike the previously mentioned parameters,  $\phi$  and  $\kappa$  are not well resolved (Figs 10a and d, respectively). This is evident from their respective histograms, nearly flat and with maxima far from the true values. In conclusion,



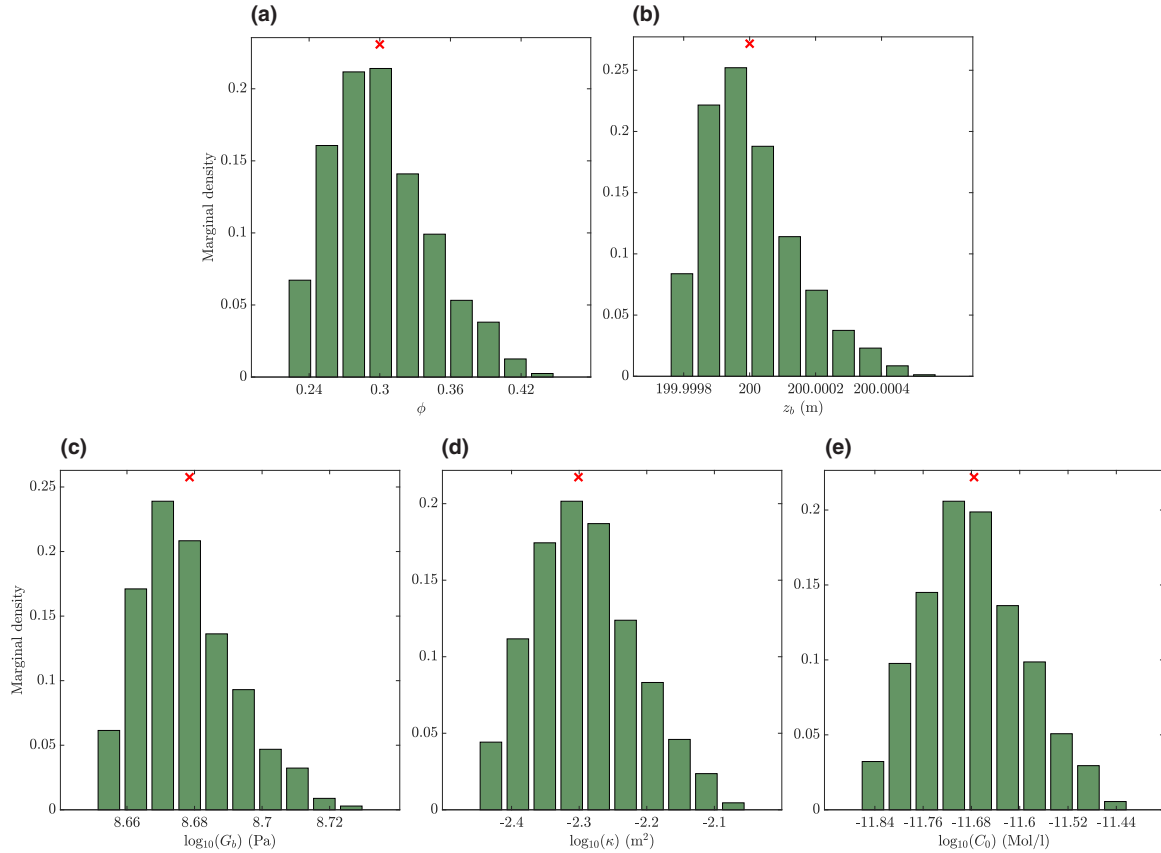


**Figure 11** Histograms of the basement porosity (a), the depth (b), the shear modulus (c), the permeability (d) and the salinity (e) for the inversion of electric data. The red cross indicates the true value for each parameter.

the only reliable parameters in this inversion case are  $z_b$  and  $G_b$ .

The inversion of the electric data led to significantly improved results. In this case, the optimal value of  $\gamma$  is 0.75 (corresponding to  $\delta = 5$ ), but the inversion worked with  $\gamma = 2$ , using  $8 \times 10^5$  iterations as in the seismic case. As the results of the inversion of the electric data set do not differ significantly from the joint case, we only display the histograms of the model parameters. These parameters were all constrained in this inversion case (Fig. 11a–e). All of them are fairly bell-shaped and their maxima are very close to the true values. In Table 2, we compare the parameters' estimate values and uncertainties to the true values used to build the synthetic data. Here it can be clearly observed how the inversion of electric data alone performs better than the corresponding of seismic data alone. Besides being able to retrieve one more model parameter, the mean values estimated are closer to the true values, and the uncertainty ranges systematically smaller. For example, the true value of the permeability expressed as  $\log_{10}(k[m2])$  is  $-11.68$ . The inversion of seismic data results

in the range of  $[-12.49, -9.69]$  of 68% probability (i.e. one standard deviation), whereas in the electric case the range is  $[-11.76, -11.58]$ .

Finally, we consider the joint inversion of seismic and electric data. This case required  $9 \times 10^5$  iterations and a  $\gamma$  value of 0.5, smaller than in the electric case and closer to the optimal value of 0.75 mentioned above. Figure 12(a–e) shows the chains searching through the parameter space. In the case of  $\phi$ , the chains oscillate around the true value with a high amplitude but without covering the entire range defined in the prior distribution (Fig. 12a). The chains for  $z_b$  exhibit, as in the seismic case, an immediate convergence to the true value (Fig. 12b).  $G_b$ ,  $\kappa$  and  $C_0$  display tiny oscillations around the true value (Fig. 12c–e), which implies that the chains managed to constrain the parameter space into a small range within the prior pdf. The values of  $p(\mathbf{m}|\mathbf{d})$  end up being close to  $-2048$ , which is half the amount of data points (Fig. 12f), as expected.

The histograms that represent the marginal distributions of the model parameters are, as in the electric case inversion,

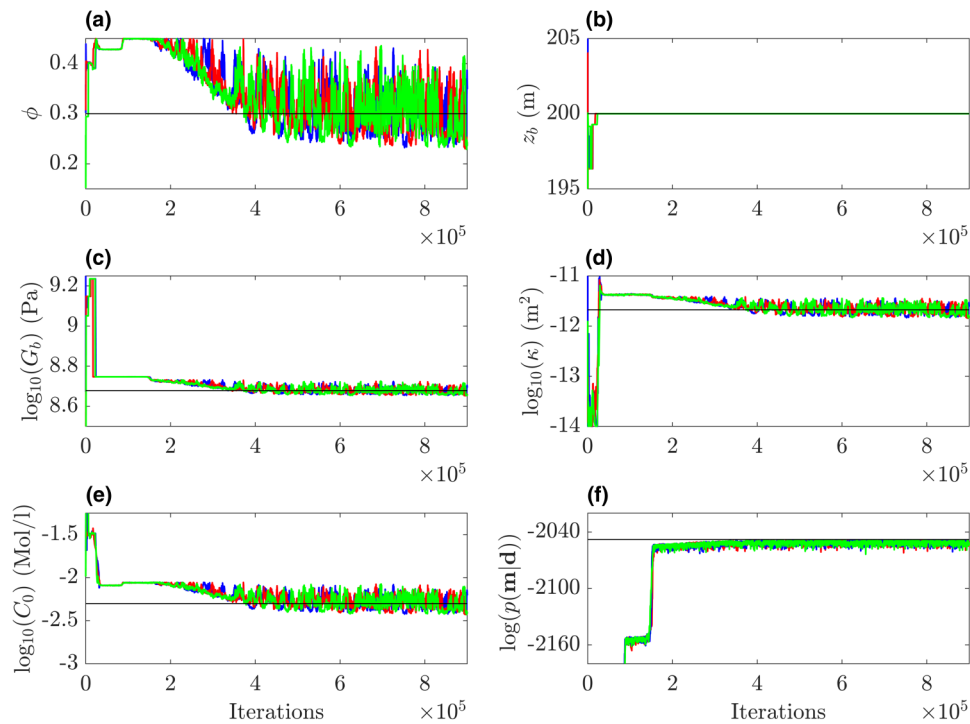


**Figure 12** (a)–(e) The convergence of the chains for each parameter, for the joint inversion (each chain is represented by the colours blue, red and green). The chains move around the prior defined for each parameter. (f) The convergence of  $\log(p(\mathbf{m}|\mathbf{d}))$  to the expected value  $-N/2$ , denoted by the solid horizontal black line.

fairly bell-shaped and with maxima almost coincident with the true values (Fig. 13). Taking a look at Table 2, the mean values of all the model parameters match the true values. Interestingly, adding the seismic data in a joint inversion scheme contributes to further constraining the uncertainty ranges of the model parameters. The uncertainty range of the permeability, following the analysis of the separate inversions, is further reduced in the joint case, reaching the interval  $[-11.76, -11.6]$  for the uncertainty ranges of the whole parameters. This result reinforces the advantages of seismoelectric data over seismic data stated in Section 1 (Mahardika *et al.* 2012; Mahardika 2013). It is clear that the electric data alone already provide a great improvement in the inversion results, but the joint case is able to slightly improve the determination of the uncertainties of the parameters.

## 7 DISCUSSION

The present study aimed at evaluating the capability of the shear horizontal (SH) seismoelectric method to retrieve relevant parameters about glacial systems. The results obtained are encouraging because they suggest that the inversion of

real solid displacement and electric field data may be feasible and informative.

The sensitivity analysis showed that, under the assumptions made regarding the glacier properties, seismoelectric data are sensitive to changes in subglacial properties like porosity, basement depth, shear modulus of the basement, permeability and salinity. Sensitivity to porosity, permeability and salinity had already been suggested by Garambois and Dietrich (2002) and confirmed by Zyserman *et al.* (2017a) and Monachesi *et al.* (2018a).

We performed sensitivity tests for different percentages of noise amplitude in the electric field (5%, 10% and 15%) and different signal-to-noise ratios (SNRs) (10, 20 and 50) for the seismic data. The least realistic cases (error of 5% for the electric field and  $\text{SNR} = 50$  for the seismic field) led in general to the sharpest minima near the true model parameter values. This may suggest that low-noise cases are the most suitable to perform the inversion. However, sharp minima imply numerical disadvantages in the calculation of multidimensional integrals with large misfit values. Thus, the more realistic data with a larger added noise of 10% error in the electric data and seismic data with  $\text{SNR} = 20$  were used for the inversion tests. We have adopted a standard model for the electric noise. This

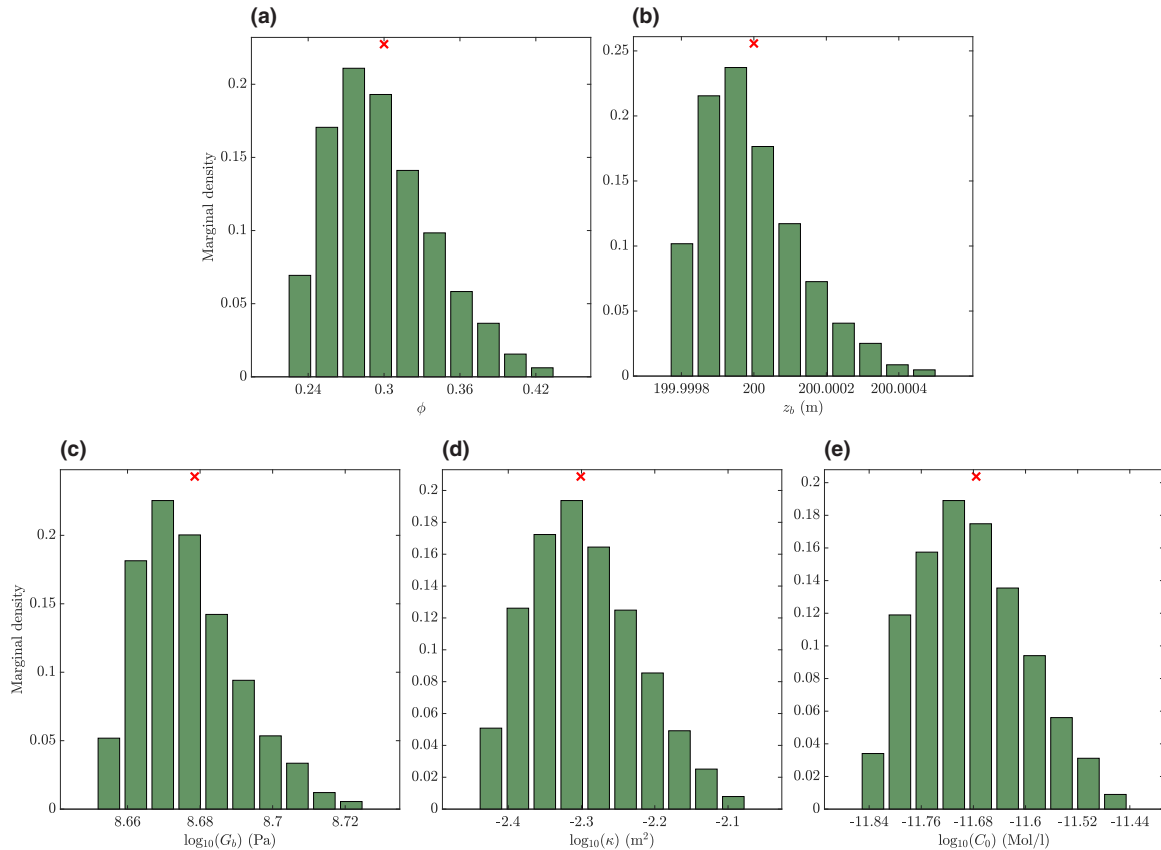


**Figure 13** Histograms of the basement porosity (a), the depth (b), the shear modulus (c), the permeability (d) and the salinity (e) for the joint inversion of seismic and electric data. The red cross indicates the true value for each parameter.

noise could be made more realistic to capture the nature of all the noise sources potentially present in a broadband electric signal. For example, the incoherent ambient noise affecting seismoelectric data will be dominated by cultural noise (e.g. power system noise), spherics (i.e. atmospheric electricity) and instrumentation (amplifier) noise. The statistics of these noise sources are expected to be essentially uniform over time (i.e. stationary noise). It is expected that the inclusion of these sources of noise would negatively impact the performance of the inversion. However, the adopted model for the electric noise could be suitable if some kind of tuned reception during seismoelectric surveys was employed, for example a narrow-band filter with central frequency equal to the peak frequency of the source.

We studied the inversion of synthetic data using two different strategies. The inversion by means of multidimensional integration allowed us to obtain marginal distributions of each model parameter. This was successful to a certain extent, because the integration range was restricted to a very narrow prior, which does not explore properly the parameter space.

This numerical problem is related to the misfit values, which have at least an order of magnitude of  $10^3$ . The exponential of such numbers is very difficult to calculate even in quadruple precision without obtaining a null result. Another drawback is that obtaining a marginal distribution curve in a very small portion of the prior demands a huge number of computations of the forward model ( $10^6$  for each parameter).

Given the limitations encountered with numerical integration, we then performed a Bayesian inversion applying a Markov chain Monte Carlo (MCMC) algorithm. This allowed us to work with the electric and seismic set separately and jointly and to obtain histograms of the marginal distributions of the model parameters in each case. In accordance to what was observed in the sensitivity analysis, the inversions were able to retrieve the relevant model parameters (with exception of the porosity and the permeability in the seismic case), in terms of marginal distributions centred around the true values. The inversion of electric data alone performed better than that of the seismic data alone, in agreement with the studies by Mahardika (2013) and Mahardika *et al.* (2012), and the joint

inversion of both data sets resulted in the best estimates of all model parameters, in terms of mean values closer to the true ones and also in uncertainty ranges that were smaller. Each case demanded no more than  $9 \times 10^5$  iterations (forward computations), which is an improvement with respect to the  $5 \times 10^6$  evaluations of the forward model of the numerical integration method. In addition, the MCMC algorithm does not require a prior range significantly close to the true values, which makes it a valuable tool to characterize glacier basement properties. Therefore, we were able to retrieve the parameters that characterize the basement properties of a glacier environment with Bayesian Monte Carlo inversion, with reasonable uncertainty estimates. It is worth to mention that the glacier bottom depth is a parameter that could be easily obtained using only the seismic traveltime combined with the known SH wave velocity of the ice. However, this independent parameter estimation entails a certain uncertainty, which we wanted to also test in the case of the electric data. Our results indicate that the inversion of electric data alone, and the joint inversion of seismic and electric data, result in smaller uncertainties of the basement depth parameter compared to the inversion of seismic data alone. As the Differential Evolution Adaptive Metropolis (DREAM) algorithm manages very well the sampling of the 5-parameter space, there is no necessity to remove this parameter from the inversion and assess it separately.

Based on our results, it would be worth to perform a field campaign and inversion of SH seismoelectric data in a glacier environment, for instance employing an ELVIS generator (Krawczyk, Polom and Beilecke 2013) for an SH source. However, a feasibility study would be suitable to understand the limitations of our approach. Such study could be based on the numerical modelling by Zyserman, Gauzellino and Santos (2010) and Zyserman *et al.* (2012). This work consists on a finite element formulation of Pride's equations in two-dimensional (2D) – that is, one employing a source/subsurface geometry configuration yielding 2D vector fields as solution to these equations – which could be implemented and afterwards incorporated in a Bayesian inversion using the DREAM algorithm. An important remark with respect to moving to 2D or 3D geometries is that the amplitudes of the wavefields will be different, which would in turn affect the results. The number of parameters to be inverted could also be larger in order to account for more complex models, thus needing parallel numerical codes implemented on clusters of computers. Nevertheless, the results accomplished in this paper definitely encourage the application and further theoretical studies on the seismoelectric method in glacier systems.


## 8 CONCLUSIONS

We have studied the seismoelectric response to a shear horizontal seismic source deployed on top of a glacier, and analysed the feasibility of recovering relevant geophysical information such as glacier depth, porosity, permeability and bulk shear modulus of the basement, as well as the salinity of the water saturating the rock. A sensitivity analysis of the parameters of interest confirmed that they were good candidates to be characterized by inverting the synthetic data. We used two different strategies to analyse the posterior marginal distributions of the free parameters aforementioned. These distributions give us information about the uncertainty with which we may be able to characterize the parameters of interest in a real field experiment. The multidimensional numerical integration was able to retrieve marginal distributions, but at the cost of using a narrow prior probability density function interval for each model parameter, and a large number of iterations. Thus, this approach may work only if sufficient good information is known prior to the experiment. In contrast, the use of the Differential Evolution Adaptive Metropolis algorithm to perform a full Bayesian inversion proved to efficiently retrieve the posterior distributions employing broader prior ranges and less number of iterations. This is a promising result that ratifies the importance of combining different geophysical methods for an improved characterization of glacial systems. Our work therefore encourages more field tests using seismoelectric data to obtain subglacial information, as well as further efforts to build efficient numerical models that account for more complex scenarios.


## ACKNOWLEDGEMENTS

We thank the two anonymous reviewers whose comments largely contributed to improve this work.

## ORCID

Franco Macchioli-Grande 

<https://orcid.org/0000-0002-6556-4718>

Fabio Zyserman  <https://orcid.org/0000-0002-2534-6521>

## REFERENCES

- Aki K. and Richards P.G. 2002. *Quantitative Seismology*, 2nd edn. Mill Valley, CA: University Science Books.
- Archie G.E. 1942. The electrical resistivity log as an aid in determining some reservoir characteristics. *Transactions of the American*

- Institute of Mining Metallurgical and Petroleum Engineers* 1, 54–62.
- Bonnetier E., Triki F. and Xue Q. 2019. An inverse problem for an electroseismic model describing the coupling phenomenon of electromagnetic and seismic waves. *Inverse Problems* 35, 1–20.
- Bordes C. 2005. *Etude expérimentale des phénomènes transitoires sismo-électromagnétiques: Mise en oeuvre au laboratoire souterrain à bas bruit de rustrel*, PhD thesis, Université Joseph Fourier, Grenoble 1, France.
- Bordes C., Sénéchal P., Barrière J., Brito D., Normandin E. and Jougnot D. 2015. Impact of water saturation on seismoelectric transfer functions: a laboratory study of coseismic phenomenon. *Geophysical Journal International* 200, 1317–1335.
- Brandt S. 1989. *Statistical and Computational Methods in Data Analysis*. Elsevier.
- Butler K.E., Kulesa B. and Pugin A.J. 2018. Multimode seismoelectric phenomena generated using explosive and vibroseis sources. *Geophysical Journal International* 213, 836–850.
- Carcione J., Seriani G. and Gei D. 2003. Acoustic and electromagnetic properties of soil saturated with salt water and NAPL. *Journal of Applied Geophysics* 52, 177–191.
- Chen J., Hoversten G.M., Vasco D., Rubin Y. and Hou Z. 2007. A Bayesian model for gas saturation estimation using marine seismic AVA and CSEM data. *Geophysics* 72, WA85–WA95.
- Chen J. and Yang Y. 2013. Inverse problem of electro-seismic conversion. *Inverse Problems* 29, 1–15.
- Collins J., Frank S. and Metzler A. 2016. Elastic parabolic equation and normal mode solutions for seismo-acoustic propagation in underwater environments with ice covers. *The Journal of the Acoustical Society of America* 139, 2672.
- Devi M., Garambois S., Brito D., Dietrich M., Poydenot V. and Bordes C. 2018. A novel approach for seismoelectric measurements using multielectrode arrangements: II—laboratory measurements. *Geophysical Journal International* 214, 1783–1799.
- Dietrich M., Devi M., Garambois S., Brito D. and Bordes C. 2018. A novel approach for seismoelectric measurements using multielectrode arrangements – I: theory and numerical experiments. *Geophysical Journal International* 215, 61–80.
- Dupuy B., Garambois S. and Virieux J. 2016. Estimation of rock physics properties from seismic attributes — Part 1: strategy and sensitivity analysis. *Geophysics* 80, M35–M53.
- Dzieran L., Thorwart M., Rabbel W. and Ritter O. 2019. Quantifying interface responses with seismoelectric spectral ratios. *Geophysical Journal International* 217, 108–121.
- Fiorentino E., Toussaint R. and Jouniaux L. 2017. Two-phase lattice Boltzmann modelling of streaming potentials: influence of the gas-water interface on the electrokinetic coupling. *Geophysical Journal International* 208, 1139–1156.
- Gao Y., Huang F. and Hu H. 2017a. Comparison of full and quasi-static seismoelectric analytically based modeling. *Journal of Geophysical Research: Solid Earth* 122, 8066–8106.
- Gao Y., Huang F. and Hu H. 2017b. Seismoelectric responses to an explosive source in a fluid above a fluid-saturated porous medium. *Journal of Geophysical Research: Solid Earth* 122, 7190–7218.
- Gao Y., Wang D., Yao C., Guan W., Hu H., Zhang W. et al. 2019. Simulation of seismoelectric waves using finite-difference frequency-domain method: 2D SHTE mode. *Geophysical Journal International* 216, 414–438.
- Garambois S. and Dietrich M. 2002. Full waveform numerical simulations of seismoelectromagnetic wave conversions in fluid-saturated stratified porous media. *Journal of Geophysical Research* 107, ESE 5-1–ESE 5-18.
- Gelman A. and Rubin D.B. 1992. Inference from iterative simulation using multiple sequences. *Statistical Science* 7, 457–472.
- Gilks W.R., Richardson S. and Spiegelhalter D. 1995. *Markov Chain Monte Carlo in Practice*. Chapman and Hall/CRC.
- Grobbe N. and Slob E. 2016. Seismo-electromagnetic thin-bed responses: natural signal enhancements? *Journal of Geophysical Research: Solid Earth* 121, 2460–2479.
- Guan W., Hu H. and Wang Z. 2013. Permeability inversion from low-frequency seismoelectric logs in fluid-saturated porous formations. *Geophysical Prospecting* 61, 120–133.
- Guan W., Shi P. and Hu H. 2018. Contributions of poroelastic-wave potentials to seismoelectromagnetic wavefields and validity of the quasi-static calculation: a view from a borehole model. *Geophysical Journal International* 212, 458–475.
- Gueguen Y. and Palciauskas V. 1994. *Introduction to the Physics of Rocks*, Princeton University Press.
- Haartsen M.W. and Pride S. 1997. Electro-seismic waves from point sources in layered media. *Journal of Geophysical Research* 102, 24,745–24,769.
- Hahn T. 2005. Cuba—library for multidimensional numerical integration. *Computer Physics Communications* 168, 78–95.
- Haines S.S., Guitton A. and Biondi B. 2007a. Seismoelectric data processing for surface surveys of shallow targets. *Geophysics* 72, G1–G8.
- Haines S.S., Guitton A. and Biondi B. 2007b. Seismoelectric imaging of shallow targets. *Geophysics* 72, G9–G20.
- Haines S.H. and Pride S.R. 2006. Seismoelectric numerical modeling on a grid. *Geophysics* 71, 57–65.
- Hassan A.E., Bekhit H.M. and Chapman J.B. 2009. Using Markov Chain Monte Carlo to quantify parameter uncertainty and its effect on predictions of a groundwater flow model. *Environmental Modelling & Software* 24, 749–763.
- Holzhauser J., Brito D., Bordes C., Brun Y. and Guatarbes B. 2017. Experimental quantification of the seismoelectric transfer function and its dependence on conductivity and saturation in loose sand. *Geophysical Prospecting* 65, 1097–1120.
- Hu H. and Gao Y. 2011. Electromagnetic field generated by a finite fault due to electrokinetic effect. *Journal of Geophysical Research: Solid Earth* 116, no. B8.
- Hu H., Guan W. and Harris J. 2007. Theoretical simulation of electroacoustic borehole logging in a fluid-saturated porous formation. *The Journal of the Acoustical Society of America* 122, 135–145.
- Hu H. and Liu J. 2002. Simulation of the converted electric field during acoustoelectric logging. 72nd SEG Annual International meeting, Expanded Abstracts, 348–351.
- Hu H., Wang J. and Guan W. 2015. Experimental measurements of seismoelectric signals in borehole models. *Geophysical Journal International* 203, 1937–1945.

- Jardani A., Revil A., Slob E. and Söllner W. 2010. Stochastic joint inversion of 2D seismic and seismoelectric signals in linear poroelastic materials: a numerical investigation. *Geophysics* **75**, N19–N31.
- Jardani A. and Revil A. 2015. Seismoelectric couplings in a poroelastic material containing two immiscible fluid phases. *Geophysical Journal International* **202**, 850–870.
- Jeffreys H. 1998. *The Theory of Probability*. Oxford University Press.
- Johnson D.L., Koplik J. and Dashen R. 1987. Theory of dynamic permeability in fluid saturated porous media. *Journal of Fluid Mechanics* **176**, 379–402.
- Jougnot D., Rubino J., Carbajal M.R., Linde N. and Holliger K. 2013. Seismoelectric effects due to mesoscopic heterogeneities. *Geophysical Research Letters* **40**, 2033–2037.
- Jouniaux L. and Zyserman F. 2016. A review on electrokinetically induced seismo-electrics, electro-seismics, and seismo-magnetics for Earth sciences. *Solid Earth* **7**, 249–284.
- Kalscheuer T., De los Ángeles García Juanatey M., Meqbel N. and Pedersen L.B. 2010. Non-linear model error and resolution properties from two-dimensional single and joint inversions of direct current resistivity and radiomagnetotelluric data. *Geophysical Journal International* **182**, 1174–1188.
- Krawczyk C., Polom U. and Beilecke T. 2013. Shear-wave reflection seismics as a valuable tool for near-surface urban applications. *The Leading Edge* **32**, 253–263.
- Kröger B., Yaramanci U. and Kemna A. 2014. Numerical analysis of seismoelectric wave propagation in spatially confined geological units. *Geophysical Prospecting* **62**, 133–147.
- Kulesa B., Murray T. and Rippin D. 2006. Active seismoelectric exploration of glaciers. *Geophysical Research Letters* **33**, L07503.
- Liu Z., Yuan L., Zhang X., Liu Z. and Wu H. 2008. A laboratory seismoelectric measurement for the permafrost model with a frozen-unfrozen interface. *Geophysical Research Letters* **35**, L21404.
- Løseth L., Pedersen H., Ursin B., Amundsen L. and Ellingsrud S. 2006. Low-frequency electromagnetic fields in applied geophysics: waves or diffusion? *Geophysics* **71**, W29–W40.
- Mahardika H. 2013. *Coupled hydromechanical and electromagnetic responses in unsaturated porous media: theory, observation, and numerical simulations*. PhD thesis, Colorado School of Mines, USA.
- Mahardika H., Revil A. and Jardani A. 2012. Waveform joint inversion of seismograms and electrograms for moment tensor characterization of fracking events. *Geophysics* **77**, ID23–ID39.
- Mavko G., Mukerji T. and Dvorkin J. 2009. *The Rock Physics Handbook: Tools for Seismic Analysis of Porous Media*. Cambridge University Press.
- Monachesi L., Rubino G., Rosas-Carbajal M., Jougnot D., Linde N., Quintal B. et al. 2015. An analytical study of seismoelectric signals produced by 1D mesoscopic heterogeneities. *Geophysical Journal International* **201**, 329–342.
- Monachesi L., Zyserman F. and Jouniaux L. 2018a. An analytical solution to assess the SH seismoelectric response of the vadose zone. *Geophysical Journal International* **213**, 1999–2019.
- Monachesi L., Zyserman F. and Jouniaux L. 2018b. SH seismoelectric response of a glacier: an analytic study. *Journal of Geophysical Research: Earth Surface* **123**, 2135–2156.
- Mosegaard K. and Tarantola A. 1995. Monte Carlo sampling of solutions to inverse problems. *Journal of Geophysical Research: Solid Earth* **100**, 12431–12447.
- Mosegaard K. and Tarantola A. 2002. Probabilistic approach to inverse problems. *International Geophysics Series* **81**, 237–268.
- Munch F.D. and Zyserman F.I. 2016. Detection of non-aqueous phase liquid contamination by SH-TE seismoelectrics: a computational feasibility study. *Journal of Applied Geophysics* **130**, 8–22.
- Overbeek J.T.G. 1952. Electrochemistry of the double layer. In: *Colloid Science, Irreversible Systems*, Vol. 1 (ed. H. R. Kruyt), pp. 115–193. Elsevier.
- Peng R., Di B., Wei J., Ding P., Zhao J., Pan X. et al. 2017. Experimental study of the seismoelectric interface response in wedge and cavity models. *Geophysical Journal International* **210**, 1703–1720.
- Petrenko V. and Whitworth R. 1999. *Physics of Ice*. Clarendon Press.
- Polom U., Hofstede C., Diez A. and Eisen O. 2014. First glacier-vibro-seismic experiment - results from cold firn of Colle Gnifetti. *Near Surface Geophysics* **12**, 494–504.
- Press W., Teukolsky S., Vetterling W. and Flannery B. 2007. *Numerical Recipes: The Art of Scientific Computing*, 3rd edn. Cambridge University Press.
- Pride S. 1994. Governing equations for the coupled electromagnetics and acoustics of porous media. *Physical Review B Condensed Matter* **50**, 15678–15695.
- Pride S. and Garambois S. 2005. Electro-seismic wave theory of Frenkel and more recent developments. *Journal of Engineering Mechanics* **131**, 697–706.
- Pride S.R. 2005. Relationships between seismic and hydrological properties. In: *Hydrogeophysics* (eds Y. Rubin and S.S. Hubbard), pp. 253–291. Springer.
- Rapetti F. and Rousseaux G. 2014. On quasi-static models hidden in Maxwell's equations. *Applied Numerical Mathematics* **79**, 92–106.
- Ren H., Huang Q. and Chen X. 2016. Existence of evanescent electromagnetic waves resulting from seismoelectric conversion at a solid-porous interface. *Geophysical Journal International* **204**, 147–166.
- Ren H., Huang Q. and Chen X. 2018. Quantitative understanding on the amplitude decay characteristic of the evanescent electromagnetic waves generated by seismoelectric conversion. *Pure and Applied Geophysics* **175**, 2853–2879.
- Revil A., Jardani A., Sava P. and Haas A. 2015. *The Seismoelectric Method: Theory and Application*. Wiley Blackwell.
- Revil A. and Mahardika H. 2013. Coupled hydromechanical and electromagnetic disturbances in unsaturated porous materials. *Water Resources Research* **49**, 744–766.
- Robinson E.A. and Treitel S. 2000. *Geophysical Signal Analysis*. Society of Exploration Geophysicists.
- Rosas-Carbajal M., Linde N., Kalscheuer T. and Vrugt J.A. 2014. Two-dimensional probabilistic inversion of plane-wave electromagnetic data: methodology, model constraints and joint inversion with electrical resistivity data. *Geophysical Journal International* **196**, 1508–1524.
- Rosas-Carbajal M., Linde N., Peacock J., Zyserman F., Kalscheuer T. and Thiel S. 2015. Probabilistic three-dimensional time-lapse inversion of magnetotelluric data to infer mass transfer in a geothermal system. *Geophysical Journal International* **203**, 1946–1960.

- Sambridge M. and Drijkoningen G. 1992. Genetic algorithms in seismic waveform inversion. *Geophysical Journal International* **109**, 323–342.
- Sambdrige M. and Mosegaard K. 2002. Monte Carlo methods in geophysical inverse problems. *Reviews of Geophysics* **40**, 1–29.
- Santos J., Ravazzoli C., Gauzellino P. and Carcione J. 2005. Numerical simulation of ultrasonic waves in reservoir rocks with patchy saturation and fractal petrophysical properties. *Computational Geosciences* **9**, 1–27.
- Santos J., Ravazzoli C., Gauzellino P., Carcione J. and Cavallini F. 2004. Simulation of waves in poro-viscoelastic rocks saturated by immiscible fluids. numerical evidence of a second slow wave. *Journal of Computational Acoustics* **12**, 1–21.
- Santos J.E. 2009. Finite element approximation of coupled seismic and electromagnetic waves in fluid-saturated poroviscoelastic media. *Numerical Methods for Partial Differential Equations* **27**, 351–386.
- Schön J. 1996. *Physical Properties of Rocks: Fundamentals and Principles of Petrophysics*, Vol. 18. Elsevier.
- Sen M.K. and Stoffa P.L. 1992. Rapid sampling of model space using genetic algorithms: examples from seismic waveform inversion. *Geophysical Journal International* **108**, 281–292.
- Siegert M.J., Kulesa B., Bougamont M., Christoffersen P., Key K., Andersen K.R. *et al.* 2018. Antarctic subglacial groundwater: a concept paper on its measurement and potential influence on ice flow. *Geological Society, London, Special Publications* **461**, 197–213.
- Tarantola A. 2005. *Inverse Problem Theory and Methods for Model Parameter Estimation*, Vol. 89. SIAM.
- Tarantola A. and Valette B. 1982. Inverse problems = quest for information. *Journal of Geophysics* **50**, 150–170.
- Ter Braak C.J. 2006. A Markov chain Monte Carlo version of the genetic algorithm differential evolution: easy Bayesian computing for real parameter spaces. *Statistics and Computing* **16**, 239–249.
- Vrugt J., ter Braak C., Diks C., Robinson B., Hyman J. and Higdon D. 2009. Accelerating Markov chain Monte Carlo simulation by differential evolution with self-adaptive randomized subspace sampling. *International Journal of Nonlinear Sciences and Numerical Simulation* **10**, 273–290.
- Warden S., Garambois S., Jouniaux L., Brito D., Sailhac P. and Bordes C. 2013. Seismoelectric wave propagation numerical modeling in partially saturated materials. *Geophysical Journal International* **194**, 1498–1513.
- Warden S., Garambois S., Sailhac P., Jouniaux L. and Bano M. 2012. Curvelet-based seismoelectric data processing. *Geophysical Journal International* **190**, 1533–1550.
- Zyserman F., Gauzellino P. and Santos J. 2010. Finite element modeling of SHTE and PSVTM electroseisms. *Journal of Applied Geophysics* **72**, 79–91.
- Zyserman F., Gauzellino P. and Santos J. 2012. Numerical evidence of gas hydrate detection by means of electroseisms. *Journal of Applied Geophysics* **86**, 98–108.
- Zyserman F., Jouniaux L., Warden S. and Garambois S. 2015. Borehole seismoelectric logging using a shear-wave source: possible application to CO<sub>2</sub> disposal? *International Journal of Greenhouse Gas Control* **33**, 82–102.

- Zyserman F., Monachesi L. and Jouniaux L. 2017a. Dependence of shear wave seismoelectricity on soil textures: a numerical study in the vadose zone. *Geophysical Journal International* **208**, 918–935.
- Zyserman F., Monachesi L. and Jouniaux L. 2017b. Reply to ‘Comment on “Dependence of shear wave seismoelectricity on soil textures: a numerical study in the vadose zone by F.I. Zyserman, L.B. Monachesi and L. Jouniaux” by Revil, A’. *Geophysical Journal International* **210**, 1652–1658.

## APPENDIX: FINAL SOLUTIONS FOR $u_x$ , $E_x$ AND $H_y$ .

The final solution for the solid displacement  $u_x$  is given by (Monachesi *et al.* 2018b):

$$u_x(z) = \begin{cases} -\frac{F^s}{i\lambda_{ice} G_{ice}} e^{i\lambda_{ice} z} + \sum_{n=1}^{\infty} U_x^{R, z_b, (n)} e^{-i\lambda_{ice}(z-z_b)} \\ + \sum_{n=1}^{\infty} U_x^{R, 0, (n)} e^{i\lambda_{ice} z}, & 0 \leq z \leq z_b, \\ \sum_{n=1}^{\infty} U_{s,x}^{(n)} e^{i\lambda_b(z-z_b)}, & z \geq z_b, \end{cases} \quad (A1)$$

where:

$$U_x^{R, z_b, (n)} = \frac{iF^s (\lambda_{ice} G_{ice} - \lambda_b G_b)^n e^{i(2n-1)\lambda_b z_b}}{\lambda_{ice} G_{ice} (\lambda_{ice} G_{ice} + \lambda_b G_b)^n}, \quad (A2)$$

$$U_x^{R, 0, (n)} = \frac{iF^s (\lambda_{ice} G_{ice} - \lambda_b G_b)^n e^{i2n\lambda_{ice} z_b}}{\lambda_{ice} G_{ice} (\lambda_{ice} G_{ice} + \lambda_b G_b)^n}, \quad (A3)$$

$$U_{s,x}^{(n)} = \frac{2iF^s (\lambda_{ice} G_{ice} - \lambda_b G_b)^{(n-1)} e^{i(2n-1)\lambda_{ice} z_b}}{(\lambda_{ice} G_{ice} + \lambda_b G_b)^n}. \quad (A4)$$

In these equations,  $\lambda_{ice}$  and  $\lambda_b$  are the S-wave seismic wave numbers of the glacier and basement, respectively, and are given by

$$\lambda_{ice} = \omega \sqrt{\frac{\rho_{ice}}{G_{ice}}}, \quad \lambda_b = \omega \sqrt{\frac{1}{G_b} \left( \rho_b - \frac{\rho_w^2}{g_0 - i\eta_w/(\kappa\omega)} \right)}. \quad (A5)$$

The summation appearing in equation (A1) is made over the  $n$ th reflection/transmission of the seismic wave at  $z = z_b$ .

The electric and magnetic fields are given by

$$E_x(z) = \begin{cases} A_{ice} e^{-ik_{ice} z} + B_{ice} e^{ik_{ice} z} & 0 \leq z \leq z_b, \\ A_b e^{-ik_b z} + B_b e^{ik_b z} - \frac{k_b^2 e^{i\lambda_b(z-z_b)}}{(k_b^2 - \lambda_b^2) \sigma_b} \sum_{n=1}^{\infty} J_v^{(n)} & z \geq z_b. \end{cases} \quad (A6)$$

$$H_y(z) = \begin{cases} \frac{k_{ice}}{\omega\mu_0} A_{ice} e^{-ik_{ice}z} - \frac{k_{ice}}{\omega\mu_0} B_{ice} e^{ik_{ice}z} & 0 \leq z \leq z_b, \\ \frac{k_b}{\omega\mu_0} A_b e^{-ik_bz} - \frac{k_b}{\omega\mu_0} B_b e^{ik_bz} & \\ -\frac{i\lambda_b e^{i\lambda_b(z-z_b)}}{k_b^2 - \lambda_b^2} \sum_{n=1}^{\infty} J_v^{(n)} & z \geq z_b. \end{cases} \quad (A7)$$

The coefficients  $k_{ice} = \sqrt{-i\omega\mu_0\sigma_{ice}}$  and  $k_b = \sqrt{-i\omega\mu_0\sigma_b}$  are the electromagnetic wave numbers of ice and basement, respectively.  $J_v^{(n)}$  is the amplitude of the  $n$ th current density originated at the  $n$ th transmission of the seismic shear wave at  $z = z_b$ , and is given by

$$J_v^{(n)} = \frac{\omega \frac{\eta_w}{\kappa} L_0 \rho_w}{\left(g_0 - \frac{i\eta_w}{\omega\kappa}\right)} \frac{2F^s(\lambda_{ice} G_{ice} - \lambda_b G_b)^{(n-1)} e^{i(2n-1)\lambda_{ice}z_b}}{(\lambda_{ice} G_{ice} + \lambda_b G_b)^n}. \quad (A8)$$

Finally, the coefficients  $A_{ice}$ ,  $B_{ice}$ ,  $A_b$  and  $B_b$  are complex constants which are determined by imposing proper

conditions for the fields at the contact between both media and at the boundaries of the system. These constants are given by

$$A_{ice} = B_{ice} = \frac{k_b^2(\lambda_b - k_b)^{-1}}{2[k_{ice} \sinh(ik_{ice}z_b) + k_b \cosh(ik_{ice}z_b)]\sigma_b} \sum_{n=1}^{\infty} J_v^{(n)}, \quad (A9)$$

$$A_b = \frac{k_b^2[k_{ice} \sinh(ik_{ice}z_b) - \lambda_b \cosh(ik_{ice}z_b)]e^{ik_bz_b}}{(k_b^2 - \lambda_b^2)[k_{ice} \sinh(ik_{ice}z_b) + k_b \cosh(ik_{ice}z_b)]\sigma_b} \sum_{n=1}^{\infty} J_v^{(n)}, \quad (A10)$$

$$B_b = 0. \quad (A11)$$

Once the fields  $u_x(z, \omega)$ ,  $E_x(z, \omega)$  and  $H_y(z, \omega)$  are computed for a given depth  $z$ , the time variation of these fields is obtained by the inverse Fourier transform.